

Copyright
by
Kenneth Carter Dodd
2012

**The Thesis (or Report) Committee for Kenneth Carter Dodd
Certifies that this is the approved version of the following thesis (or report):**

**Spectroscopic Measurement of n_e and T_e Profiles using Atomic and
Kinetic Models for Argon in the Texas Helimak**

**APPROVED BY
SUPERVISING COMMITTEE:**

Supervisor:

(Name typed under line, omitting Ph.D. or Dr.)

(Name typed under line, omitting Ph.D. or Dr.)

**Spectroscopic Measurement of n_e and T_e Profiles using Atomic and
Kinetic Models for Argon in the Texas Helimak**

by

Kenneth Carter Dodd, B.S.

Thesis or Report>

Presented to the Faculty of the Graduate School of

The University of Texas at Austin

in Partial Fulfillment

of the Requirements

for the Degree of

<Name of degree as in graduate catalog, do not abbreviate>

The University of Texas at Austin

<Month year>

Dedication

<Optional: If you do not include a Dedication, delete the entire page. **Do not delete the section break below.** It is needed to initiate the printing of page numbers from the Acknowledgements page on.>

Acknowledgements

<Optional: if Acknowledgements page is not used, delete the entire page, including the following page break. **Do not delete the section break above.** It is needed to initiate the printing of page numbers from this page on.>

Abstract

Spectroscopic Measurement of n_e and T_e Profiles using Atomic and Kinetic Models for Argon in the Texas Helimak

<Student's full official name, degree sought (abbreviated)>

The University of Texas at Austin, <year>

Supervisor: <Professor's name without titles or degrees>

<Abstract: May not exceed 350 words. It should be a concise statement of the nature and content of the thesis or report.>

Table of Contents

List of Tables	ix
List of Figures	x
List of Illustrations	Error! Bookmark not defined.
CHAPTER 1: INTRODUCTION	13
1.1 Background	13
1.2 Motivation	13
1.3 Objectives	15
1.4 Organization	16
Chapter 2: Texas Helimak	18
2.1 Structure	18
Chapter 3: Data Acquisition and Processing	19
3.1 Spectrometer	19
3.2 Optical System	19
3.3 Lens, Fiber, and Spectrometer Calibration	20
3.4 Window Calibration	22
3.5 Neutral Gas Pressure Acquisition	25
3.6 Spectral Acquisition	26
3.7 Data Storage	28
3.8 Processing raw data	28
3.9 Atomic Levels and Transitions	32
Chapter 4: Using Argon Models to find n_e and T_e	35
4.1 Introducing Atomic Processes	35
4.2 Coronal and LTE Models	36
4.3 Collisional-Radiative Model	38
4.4 Argon I CR Model	40
4.5 Argon II CR Model	43

4.6 Determining <i>ne</i> and <i>Te</i>	44
4.7 First Correction for Neutral Density	46
Chapter 5: Neutral Density Profile	48
5.1 Motivation.....	48
5.2 Kinetic Model	49
5.3 Results.....	59
Chapter 6: Electron Velocity Distribution	64
6.1 Motivation.....	64
6.2 Fokker-Planck Scattering.....	65
6.3 Inelastic Scattering.....	67
6.4 Energy and Particle Balance	70
6.5 Numerical Solution for Argon I.....	71
6.6 Correction Factors.....	75
Chapter 7: Spectroscopic Profiles for <i>ne</i> and <i>Te</i>	78
7.1 Profile Calculation	78
7.2 Discussion	80
Appendix (or Appendices).....	81
Glossary	82
References.....	83

List of Tables

Table 3.1: Data used to convert the measured lines to population densities relating to the available models. One model for the Ar I levels, and one for the Ar II levels. Δt is the integration time used for each line. Wavelengths marked with * are average of two lines.	33
Table 3.2: Statistical weights used for each modeled level.	34
Table 4.1: Solutions from Ar I effective levels 6 through 9 combined into macro-state, divided by ground state density to give the relative density. Each row is electron temperature range in eV. Each column is the electron density range in $m - 3$. Values are found by multiplying by the ground state density.....	43
Table 4.2: Solutions from Ar II effective levels 13 through 15 combined into macro-state, in units of $m - 3$. Each row is electron temperature range in eV. Each column is the electron density range in $m - 3$	44
Table 6.1 Argon I Excitation Rate Corrections ($\epsilon = 11.5eV$)	76
Table 6.2 Argon II Excitation Rate Corrections ($\epsilon = 19.2eV$)	76

List of Figures

Figure 2.1: External view of Helimak and cross-section view from Texas Helimak ^[3]	18
Figure 3.1: USB-650 internal view from manual ^[6]	19
Figure 3.2: Optical system layout	20
Figure 3.3: Calibration constant K versus wavelength	22
Figure 3.4: Window calibration setup	22
Figure 3.5: Window transmission versus wavelength at x=15cm	24
Figure 3.6: Average window transmission versus position	24
Figure 3.7: USB-6008 used acquire voltage output from ionization gauge controller.	25
Figure 3.8: Labview acquisition control panel	27
Figure 3.9: Raw spectrum at absolute radial position of 1.1m, near the peak of the temperature and density of the Helimak with an integration of 200ms.	29
Figure 3.10: Calibration of the raw spectrum in figure 3.9 gives absolute radiance of light coming from Helimak plasma with an integration time of 200ms.	30
Figure 3.11: Calibrated spectrum at same radial position as figure 3.10, but with an integration time of 1000ms.	31
Figure 4.1: $A_k A_k + n e i \sigma_{kiv}$ calculated for each level in the Bogaerts model ^[4] . Values of $n e$ and $T e$ used are typical of the Helimak.	38
Figure 4.2: Level lifetimes calculated for each level in the Bogaerts model ^[4] . Values of $n e$ and $T e$ used are typical of the Helimak.	39

Figure 4.3: Energy level diagram of Ar I effective levels taken from Bogaerts ^[4] .	41
Figure 4.4: Solution of equations 4.3 and 4.4. The intersection of the two curves gives the value of ne and Te .	45
Figure 5.1: Ionization rates for Argon from Bogaerts ^[4] and Arnaud ^[12] .	48
Figure 5.2: Component of path perpendicular to z-axis of Helimak. Can intersect either inner wall or outer wall depending on θ . (a) [left] Path Intersects Inner Wall. (b) [right] Path Intersects Outer Wall.	52
Figure 5.3: Matching wall condition with floor and ceiling.	53
Figure 5.4: Integrals $M\alpha$ and $N\alpha$ plotted over a range of the parameter.	57
Figure 5.5: Discrete segment on the unit sphere.	58
Figure 5.6: Fitting function for ne or Te profiles.	60
Figure 5.7 The first moment of fx, v plotted in upper half of Helimak chamber. (a) [left] nx , normalized to average density. (b) [right] z-average of normalized nx .	62
Figure 5.8 The second moment of fx, v in the upper half of chamber. (a) [left] streamlines of flux density Γx . (b) [right] magnitude of $v = \Gamma x / nx$.	63
Figure 6.1 Energy diagram of inelastic scattering from ionization.	69
Figure 6.2 Solution electron velocity distribution fvv compared to a Maxwellian at the effective temperature.	74
Figure 6.3 The distribution in $\log fv$ versus $\epsilon = 12mev^2$	74
Figure 7.1 Profiles of Ar I calculated for three different peak electron temperatures and densities using the kinetic model of chapter 5.	78
Figure 7.2 ne and Te using the spectroscopic measurements and neutral profiles in figure 7.1. The closest match is the 10eV profile, giving an average peak Te of about 11eV.	79

CHAPTER 1: INTRODUCTION

Emission spectroscopy was used to infer excited state densities of neutral and singly ionized Argon in the Texas Helimak. The combination of spectra was used to determine a self-consistent value for the electron temperature and density of the plasma using theoretical values from collisional radiative (CR) models for both species, as well as a kinetic description of the neutral Argon gas to estimate the neutral ground state profile. Corrections are also estimated to the electron collisional excitation rates due to a non-maxwellian electron velocity distribution from inelastic collisions.

1.1 BACKGROUND

Atomic emission spectroscopy is a diagnostic tool that can give passive measurements of plasma properties. Transitions between atomic levels emit light of specific wavelengths. When analyzed with a spectrometer, the amount of light at each wavelength can give a measure of how frequently a certain transition is occurring in the plasma. The frequency of the transitions can then be related to plasma parameters through the physics of interactions between other constituents of the plasma.

1.2 MOTIVATION

This project began because of seemingly strange results seen from the Texas Helimak ^[3] between measured spectral intensities from neutral Argon (Ar I), probe measurements of electron temperature and density profiles, and predicted values obtained from a collisional radiative model for neutral Argon developed by Bogaerts et. al. ^[4]. The usefulness of this model lies in the ability to tie it to the physical quantities of the plasma, but that must be done in a self-consistent manner to be confident in the results. The method of determining neutral density used by Sciamma^[5] was used in a scan over a

small range of radial positions of the Helimak. However, the variation of the determined z-averaged neutral density was nearly a factor of four, which is much larger than expected. Several approaches were taken to try to eliminate possible causes for inconsistency.

The use of probe measurements of the electron temperature T_e and density n_e entails several possible issues as it relates to this work. One is that probe data was not available for every shot, and instead had been determined from previous shots that had similar conditions such as the input current of the toroidal field (TF) coils and vertical field (VF) coils, RF power input, and filling pressure. The ideal situation would be to have measurements of n_e and T_e for every shot they are needed. Another is the uncertainty in the measurement of n_e by probes due to their unknown effective area, which introduces an unknown systematic error.

There is also still some question of how close the electron distribution is to being Maxwellian. The probes sample the distribution near the floating potential of the plasma, $V_f = \frac{1}{2} \frac{T_e}{e} \ln(m_i/2\pi m_e)$, which for Argon is about $V_f \cong 4.7 \frac{T_e}{e}$. The excitation energies of the observed states of neutral Argon are around 11.5eV. For a $T_e=10\text{eV}$ plasma, the part of the distribution the probe measurements and spectroscopic measurements sample are fairly different.

Finally, the profile of the neutral Argon density is not known a priori. The neutral density was initially estimated from ionization gauge pressure readings, but if the density was not uniform throughout the vacuum chamber, then inferences from the excited states using that pressure reading would not be correct.

1.3 OBJECTIVES

The overall objective is to obtain self-consistent values of n_e , T_e , and neutral density (n^{+0}), with measurements of line emission intensity based on the available atomic model [4]. Given a measurement of the absolute line emission intensity from one of the modeled excited state of neutral Argon, the three unknowns n_e , T_e , and n_{ArI} are dependent. Conceptually, this means that three relations are needed to solve them uniquely.

In principle, one could use two separate excited levels of neutral Argon to determine the electron temperature since the ratio of the two levels does not depend on either neutral density or electron density, but does depend on the electron temperature through the excitation rates. However, it was found that the observed lines did not exhibit enough independent behavior to resolve the effect of electron temperature. It is thought that the energies of these levels are too close together to see the temperature dependence over the noise of the observation system.

Instead, a second relation involving n_e and T_e was obtained by measuring line emissions from the ion Ar II, and using the atomic data for Ar II used by Sciamma [5]. The excitation energies of the observed levels of Ar II are around 19.2eV. This gives an energy separation from the Ar I levels of about 7.7eV, which should be large enough to see the temperature dependence of the excitation rates with the available equipment. If the electron density is approximately equal to the ion density $n_e = n_{ArII}$, then the two models could be used to solve for n_e and T_e , given that n_{ArI} could be known.

To determine n_{ArI} , it was decided that a kinetic model for a neutral, low density gas would need to be developed and coded for the Helimak's geometry, boundary conditions, and source profiles. While the kinetic model itself would also depend on n_e

and T_e for inputs to the ionization rates, the combination of the three models should then provide a self-consistent result.

Once these tasks are completed, the n_e and T_e obtained could be compared to those obtained from the Langmuir probes, and possibly provide a method to calibrate for the systematic error in the density measurements.

A secondary object was to try to account for the effect of inelastic collisions, which might lead to a non-Maxwellian electron distribution. In an attempt to correct for this in the spectroscopic measurements, a solution was sought to the Fokker-Plank equation using the Landau-Boltzmann collision operator with the addition of inelastic collision and ionization operators. The solution was then used to make a crude correction to electron collision rates without needing to re-calculate the rates that were tabulated using a Maxwellian distribution. These corrections would be used in the models to alter the excitation rates of both Ar I and Ar II as well as the ionization rates used in the kinetic model of n_{ArI} .

1.4 ORGANIZATION

The thesis is divided into seven chapters. Chapter 2 describes the Texas Helimak. Chapter 3 describes the equipment used for spectroscopic measurements, calibration methods, data acquisition software, and the processing of the raw data. Chapter 4 explains the collisional radiative models used for Ar I and Ar II and how they would be used to determine n_e and T_e . Chapter 5 details the kinetic model developed to estimate the neutral density profile in the Helimak. Chapter 6 explains the inclusion of inelastic collisions on the electron distribution. Chapter 7 presents the resulting self-consistent

profile of n_e and T_e that was determined and compares it to that found by Langmuir probes, and suggests future related work.

Chapter 2: Texas Helimak

The Texas Helimak^[3] has an axisymmetric, helical magnetic field. The Helimak was built to study turbulent transport in curved magnetic field geometry such as those found in the edge of a Tokamak plasma. The plasma terminates on end plates at the top and bottom which allow probes to measure these properties directly. The vacuum chamber also has several viewports which allow spectroscopic measurements to be taken in chord integrals through the plasma.

2.1 STRUCTURE

The Helimak vacuum chamber is a toroid with a rectangular cross section. The plasma is produced by microwave RF input power up to 6kW at a frequency of $f = 2.45$ GHz, which causes electron-cyclotron heating (ECH) at $\omega_{ce} = eB/m$ as well as at the upper-hybrid resonance $\omega_{uh}^2 = \omega_{ce}^2 + \omega_{pe}^2$ at other locations in the plasma.

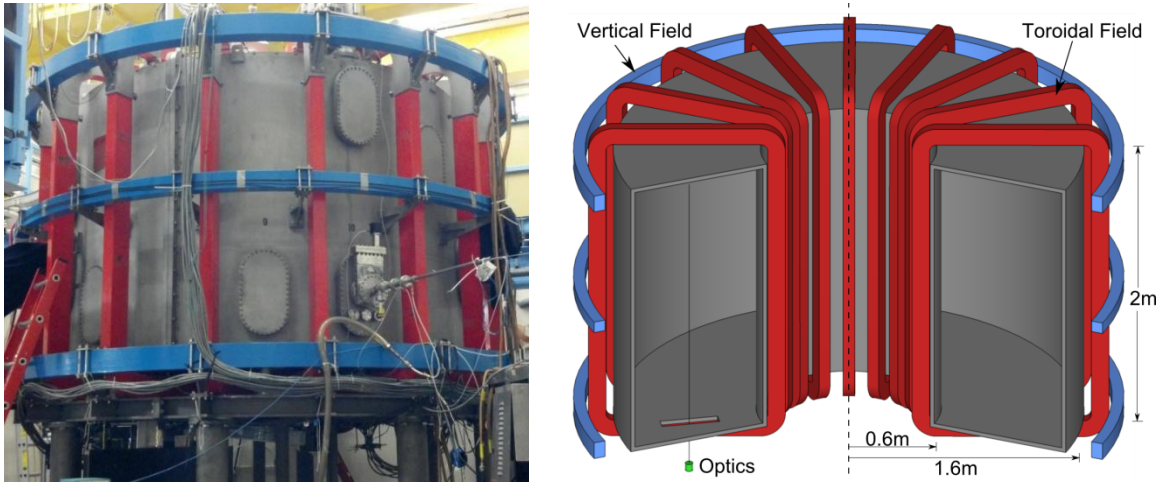


Figure 2.1: External view of Helimak and cross-section view from Texas Helimak^[3]

Chapter 3: Data Acquisition and Processing

The data acquisition includes the optical system, control software, data storage, and initial processing.

3.1 SPECTROMETER

The spectrometer used was produced by Ocean Optics, model USB-650. It has a wavelength range of 349nm to 999nm, with a resolution of 2nm (FWHM). It has 651 pixels and an adjustable integration time from 3ms to 65s.

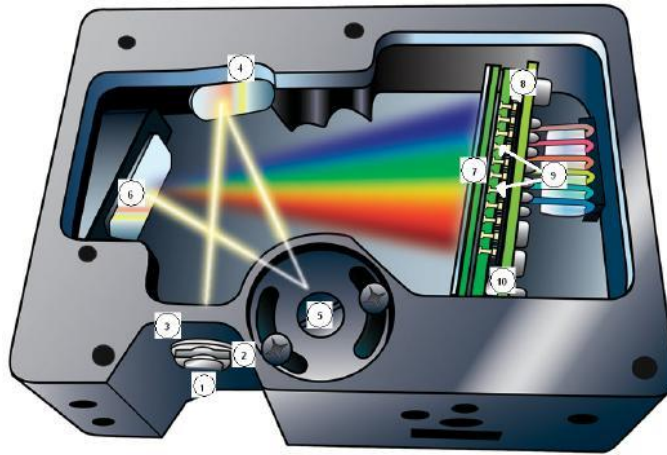


Figure 3.1: USB-650 internal view from manual ^[6]

3.2 OPTICAL SYSTEM

The Helimak plasma was viewed through an optical port on the bottom of the machine as seen in figure 3.2. The physical window was approximately 40cm wide, and gives a maximum effective viewing range of about 35cm for a 50mm lens. The lens was mounted on a ruled linear track which also served as a position measurement. The lens was connected to the spectrometer through an optical fiber of approximately 2m in length.

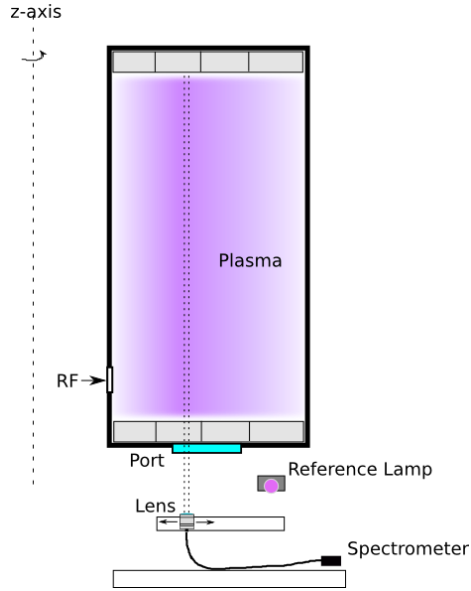


Figure 3.2: Optical system layout

The starting position of the track was measured from the inner radius of the Helimak chamber using a plumb line from the chamber to the track's position. The inner radius of the chamber was also measured to give the starting radius of the track. There were two track segments. The starting radius of the second track was also measured relative to the first track.

This allows for a measurement of only one radial position per experimental shot. The position of the lens can be changed between shots to build of a radial profile of measurements, assuming the conditions are the same for all shots.

3.3 LENS, FIBER, AND SPECTROMETER CALIBRATION

Calibration of the combination of the lens, fiber optic, and the spectrometer where done by taking the setup and measuring a known calibrated lamp, which has performed by William Rowan using a Lab-Sphere source at MIT. The known

spectral radiance profile of the lamp $L(\lambda)$, given in units of $[\frac{W}{m^2 sr nm}]$, was used to calculate a calibration constant $K(\lambda)$. A measurement of the lab-sphere emissions was made using the combination of lens, optical fiber, and spectrometer. The calibration constant was then determined using eq. 3.1, where $N(\lambda)$ is the number of counts at a given wavelength with background subtracted, and $L(\lambda)$ is the known radiance of the lamp at that wavelength, and Δt is the integration time used for the measurement. The constant can then be used to calculate the radiance of the plasma from the number of counts on the spectrometer for later measurements. The determined calibration is shown in figure 3.3.

$$K(\lambda) = \frac{N(\lambda)}{\Delta t L(\lambda)} \quad (3.1)$$

$$L(\lambda) = \frac{N(\lambda)}{\Delta t K(\lambda)} \quad (3.2)$$

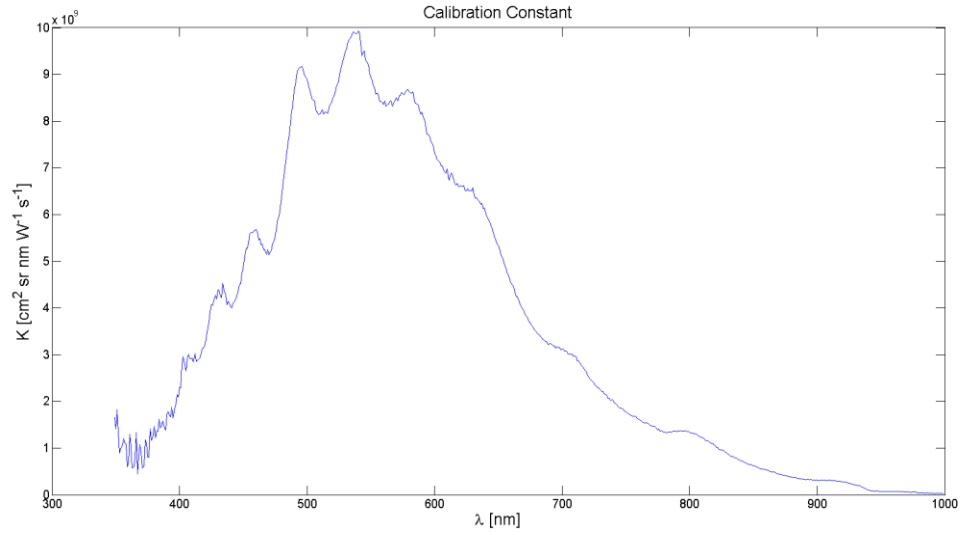


Figure 3.3: Calibration constant K versus wavelength

3.4 WINDOW CALIBRATION

The optical transmission qualities of the port window were measured as a function of position along the width of the window to account for any variations. The window also has a copper mesh screen on top of it to prevent RF power from escaping through the port. Calibration was accomplished by removing the entire window and screen and mounting in on a linear track. A reference light source was positioned on one side and the lens on the other, as seen in figure 3.4.

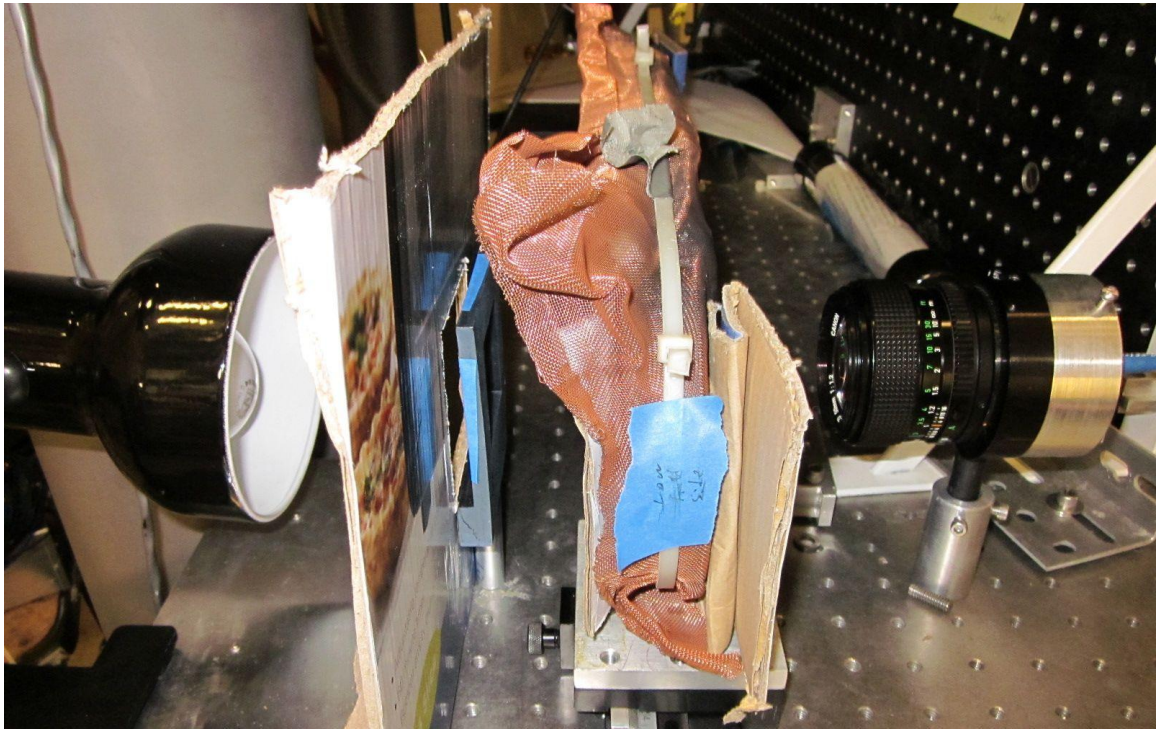


Figure 3.4: Window calibration setup

The reference light source consisted of a standard light bulb and a diffusor made a piece of paper. A measurement of the light source was made without the window in place to serve as a reference, as well as a background reference. The cardboard served to block

light to prevent the light from reflecting off of other surfaces which might contribute to the measurements.

Transmission measurements were made at 1cm increments along the length of the window. At each position, several spectra was taken and averaged together. The transmission of the window versus wavelength was calculated by dividing the measurements at each position by the measurement made without the window in place with background subtracted. That is, the transmission is $C(\lambda, x) = I(\lambda, x)/I_0(\lambda)$. A sample of the transmission profile versus wavelength can be seen in figure 3.5 measured at position of 15cm from high field side. Figure 3.6 shows average transmission over all wavelengths versus position.

This transmission factor was included in the calibration constant for the lens/fiber/spectrometer by defining a total calibration constant in eq. 3.3.

$$K_{tot}(\lambda, x) = C(\lambda, x)K(\lambda) \quad (3.3)$$

The total calibration constant could then be used as the absolute calibration of the optical system when the lens is then aimed through the same window after it was mounted back on the Helimak. This does not, however, account for any reflections from the opposite side of the vacuum chamber as there is no proper optical dump there to prevent scattered light from entering the optics. This could cause the system to over-estimate the emission of the plasma.

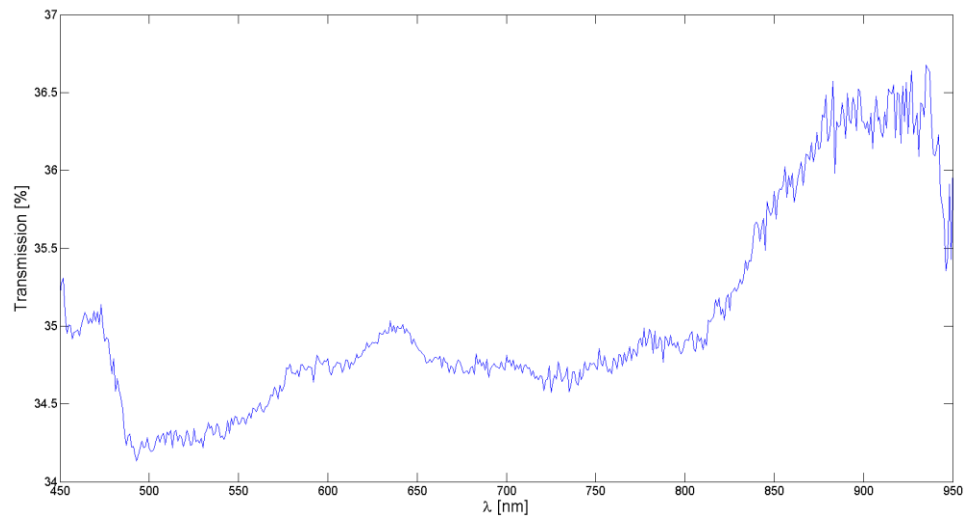


Figure 3.5: Window transmission versus wavelength at $x=15\text{cm}$

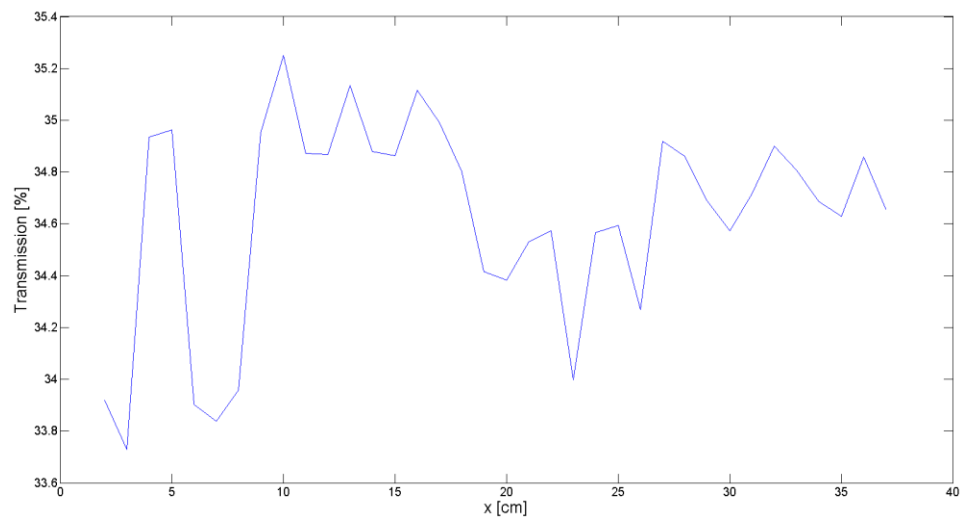


Figure 3.6: Average window transmission versus position

3.5 NEUTRAL GAS PRESSURE ACQUISITION

The neutral gas pressure was obtained from a hot filament ionization gauge which is located near the pumping system. The ionization gauge controller had a voltage output for automatic recording of the pressure. The pressure decade, in units of Torr, was given by the most significant voltage unit, and the linear scale was given by the lower significant units.

The raw voltage output was recorded by one channel of a National Instruments USB-6008 multifunction DAQ^[9] as in figure 3.7. The acquisition Labview vi recorded the conversion to pressure in Torr as well as recorded the raw voltage. Only pressure readings right before each shot was taken to avoid interference from the shot itself when the data was analyzed.

Ionization gauges are typically calibrated for measuring pressure in Nitrogen, but will measure higher or lower when measuring other gases. A correction factor must be applied to the pressure reading for other gases. For Argon this factor is 1.29^[7]. The actual pressure is then determined by dividing the recorded pressure by this correction factor.



Figure 3.7: USB-6008 used acquire voltage output from ionization gauge controller.

3.6 SPECTRAL ACQUISITION

A Labview vi was written to control and acquire data from the USB-650 spectrometer using the Ocean Optics Labview interface library. The control panel can be seen in figure 3.8. The vi allowed similar controls to the standard Ocean Optics control software, but also allowed customized actions.

The vi connected to the MDSPlus database of the Helimak control system, and used the MDSPlus shot event that is sent out at the beginning of each shot to automatically synchronize data acquisition with the shot. The signal was received several seconds before the shot began, which allowed acquisition during the entire shot that lasts approximately 30s.

The control panel allowed the user to set multiple integration times for the spectrometer to use during the shot. Each integration time was used in sequential order. After it had used one of each integration time it would start again with the first one. This allowed for frames with long integration times to be used for parts of the spectrum which are not as bright as other parts, while the shorter integration times are used for the intense parts of the spectrum which would saturate the detector for the longer integration times.

The control panel also had input fields for data related to the optical system, such as which lens and fiber were being used, the location and orientation of the lens during the shot, or other information that could be useful at a later date in analyzing the spectra. Once it finished acquiring the spectra during the shot, it would store the data in a human readable text file as. The user would then have to set it to start waiting for the next shot.

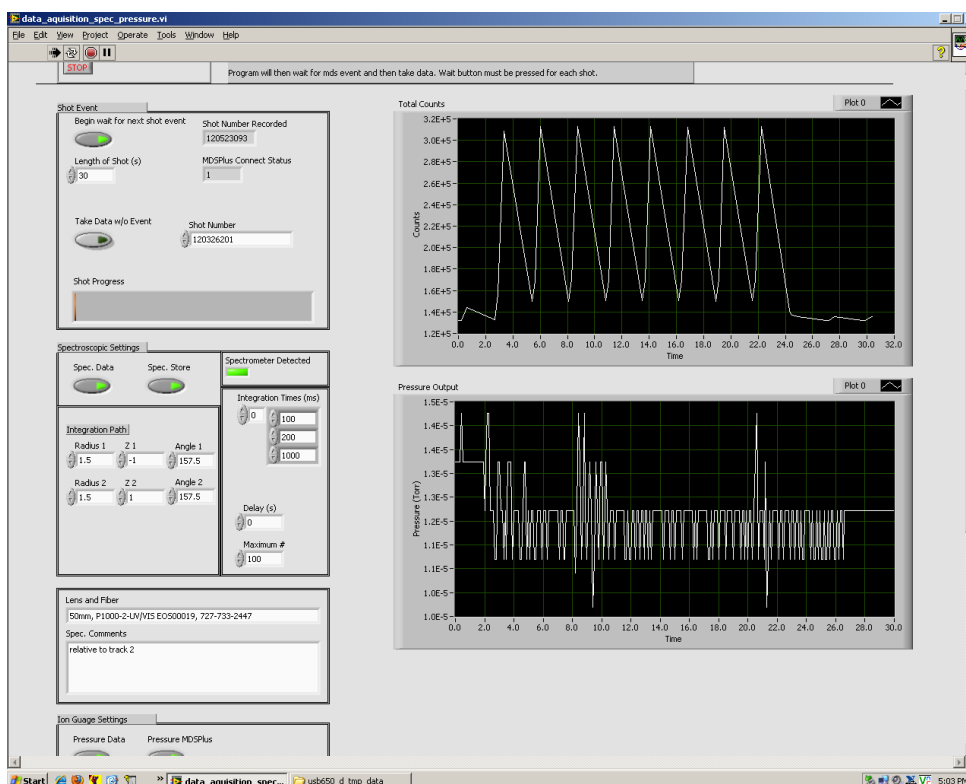


Figure 3.8: Labview acquisition control panel

In the sample screen-shot of the vi is shown in figure 3.8 there are two plots shown on the right of the control panel to summarize the results at the end of each shot. The top plot shows the total number of counts from the spectrometer summed over all wavelengths versus time. The saw-tooth pattern is a result of sequentially longer and shorter integration times. Longer integrations have more counts. The start and end of plasma formation can be seen from this plot.

The bottom plot gives the recorded pressure from the ionization gauge during the shot. Some variation of the pressure reading was observed during shots, but it is not known if this is a real pressure change or if the ionization gauge was affected by the Helimak's magnetic field or some other effect during the shot.

3.7 DATA STORAGE

After each shot the vi would write the data to a data file which had a similar structure the data would have in MDSPlus. The first line of each data segment in the file contained the MDSPlus node name the data should be put into. The second line contained the data type; either numeric=0 or string=1. The third line contained the number of dimensions of the data: either 1D or 2D. If 1D then the fourth line gave the number of lines of data before the next data entry and the fourth line starts listing the data. If 2D then the third line gives the number of lines and the fourth line gives the number of columns.

The vi would also write to a status file which contained a number representing the status of data collection. A '0' in the file meant that collection is waiting for a shot. A '-1' in the file means data collection has ended and is not waiting for any more shots. Otherwise the number in the file was equal to the shot number from which new data was collected. A script running in IDL would wait until the status file contained a new shot number, and would load the data from the corresponding data file into MDSPlus. The script would terminate when the status was set to '-1'.

MDSPlus does has a Labview interface which would have allowed the vi to load the data directly, but the interface was found to give unpredictable results. Also, the data file acted as a human readable backup of the data.

3.8 PROCESSING RAW DATA

Before the data is used to perform analysis, initial processing was done to average all the spectra of the same integration time, apply the calibration, and to convert the raw spectra into population densities of excited states for both neutral and singly ionized Argon.

Spectra were only taken into the average from the flat top operation period of each shot. There was a period of time at the beginning of each shot before which the spectra were discarded, and a period near the end after which they are discarded.

A sample spectrum with an integration time of 200ms is given in figure 3.9 after averaging over all the raw spectrum of the same integration time and subtracting the background. Figure 3.10 shows the spectrum after absolute radiance calibration is applied.

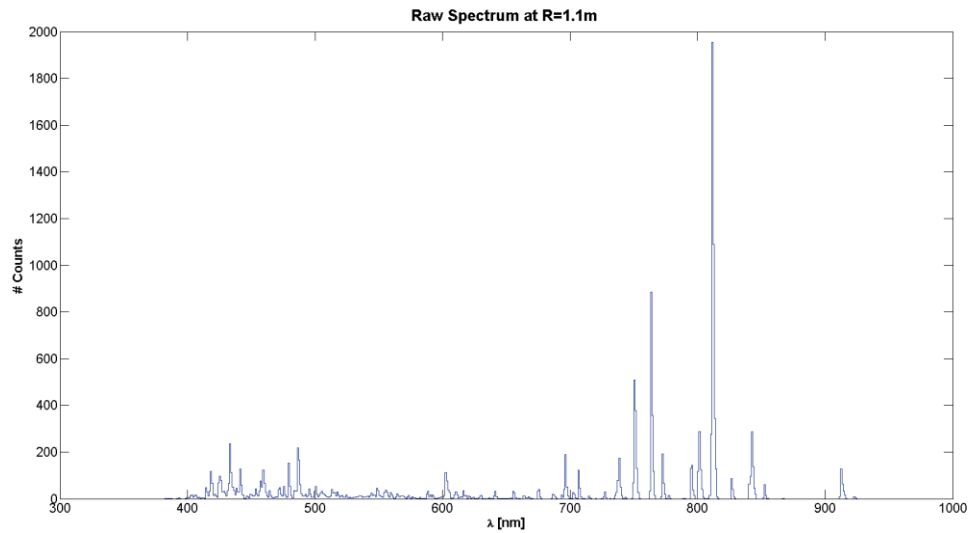


Figure 3.9: Raw spectrum at absolute radial position of 1.1m, near the peak of the temperature and density of the Helimak with an integration of 200ms.

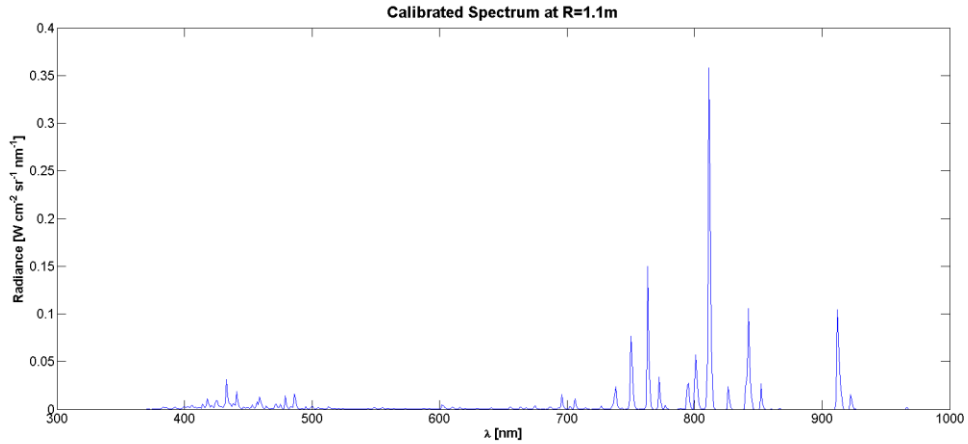


Figure 3.10: Calibration of the raw spectrum in figure 3.9 gives absolute radiance of light coming from Helimak plasma with an integration time of 200ms.

The lines below about 500nm are coming from singly ionized Argon, while the lines about 700nm come from neutral Argon. Several Hydrogen lines can also be seen between the two groups, perhaps from some residual water vapor in the vacuum chamber. When the integration time of 1000ms was used as in figure 3.11, some of the dimmer lines become more defined. However, the stronger lines have saturated the spectrometer, and the values of radiance for those lines are not correct.

The next step was to convert the spectrum into population densities for the excited states of interest. Conceptually this involves integrating over a single line to get the total radiance of that line. This was implemented by using an isolated line, integrating over that line, and dividing by the peak spectral radiance of that line which gives an effective line width: $\Delta\lambda_{eff} = \int d\lambda' L(\lambda')/L_{peak}$. This avoids issues with overlapping lines and gives the total radiance of the line in terms of the peak value: $L_{tot} = \Delta\lambda_{eff} L_{peak}$ [$W m^{-2} sr^{-1}$]. The effective line width used was $\Delta\lambda_{eff} = 2.39 nm$.

The total radiance is related to the emission from the plasma by a chord integral representing a narrow cone from the collection lens extending through the plasma:

$L_{tot} = \frac{hc}{\lambda} \int_0^l dl' \epsilon$, where ϵ is the angular photon number emission density from a single transition in $[s^{-1}sr^{-1}cm^{-3}]$. However, since the plasma should be nearly uniform in the vertical direction, the emission density should be nearly a constant. The integral would then simply be the length of the chord l multiplied by the emission density ϵ . The chord length was taken to be $l = 1.72m$.

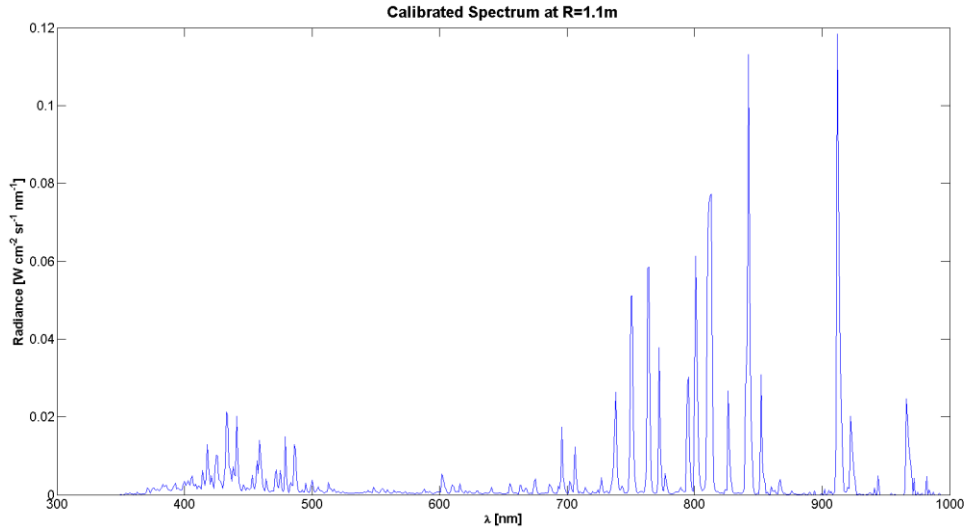


Figure 3.11: Calibrated spectrum at same radial position as figure 3.10, but with an integration time of 1000ms.

The Einstein coefficient for the transition of interest A_{ji} gives the effective frequency in $[s^{-1}]$ for the transition from excited state j to state i . It is assume the emission is isotropic which gives the emission density in terms of the population density of upper state j : $\epsilon = \frac{1}{4\pi} A_{ji} n_j$. Within the collisional-radiative models the micro states are grouped into a common state.

The population density of each microstate is found in terms of the modeled state through the fractional statistical weight: $n_j = \frac{g_j}{g_k} n_k$, where $g_k = \sum g_j$ is the sum is over all microstates of state k . The population density of one of the modeled excited states can

then be written in terms of the absolute radiance L_{tot} as measured from the plasma and the chord integral through the plasma of length l as in eq. 3.4.

$$n_k = \frac{g_k}{g_j} \frac{4\pi}{lA_{ji}} \frac{\lambda}{hc} L_{tot} \quad (3.4)$$

3.9 ATOMIC LEVELS AND TRANSITIONS

For neutral Argon, the upper state density is calculated for four of the modeled states from the Bogaerts CR model ^[4]. For singly ionized Argon, it is calculated for three states from the ADAS CR model.

For some upper states multiple lines are used in the determination of the density. Only those lines which do not ambiguously overlap with lines from other levels are used, which reduced the total number of available lines. If two lines from the same model level do overlap, then both are used with the coefficients from each micro-state added together. For levels that have more than one line measurement, the density is averaged between the results of the individual lines where each line is weighted equally. A total of sixteen lines are used and are tabulated in table 3.1.

line	λ [nm]	Ion	Upper State Term(s)	Model #	$\frac{g_j}{g_k} \frac{hc A_{ji}}{4\pi\lambda}$ [Wsr^{-1}]	Δt [ms]
1	434*	Ar II	$^3P4p \ ^4D \ ^3/2 + ^7/2$	14	2.123e-12	1000
2	442.8*		$^3P4p \ ^4D \ ^3/2 + ^5/2$	14	1.282e-12	1000
3	480.6	Ar II	$^3P4p \ ^4P \ ^5/2$	13	1.283e-12	1000
4	487.98		$^3P4p \ ^2D \ ^5/2$	15	1.600e-12	1000
5	696.5431	Ar I	$^2P_{1/2} 4p[^1/2]_1$	9	1.451e-13	1000
6	706.7218		$^2P_{1/2} 4p[^3/2]_2$	8	5.315e-14	1000
7	738.398	Ar I	$^2P_{1/2} 4p[^3/2]_2$	8	1.134e-13	1000
8	763.5106		$^2P_{3/2} 4p[^3/2]_2$	7	1.268e-13	200
9	794.8176	Ar I	$^2P_{1/2} 4p[^3/2]_1$	8	1.388e-13	1000
10	801*		$^2P_{3/2} 4p[^3/2]_2 + [^5/2]_2$	7	6.999e-14	1000
11	811*	Ar I	$^2P_{3/2} 4p[^3/2]_1 + [^5/2]_3$	7	2.990e-13	200
12	826.4522		$^2P_{1/2} 4p[^1/2]_1$	9	2.928e-13	1000
13	852.1442	Ar I	$^2P_{1/2} 4p[^3/2]_2$	8	9.675e-14	1000
14	912.2967		$^2P_{3/2} 4p[^1/2]_1$	6	3.277e-13	200
15	922.4499	Ar I	$^2P_{3/2} 4p[^3/2]_2$	7	2.156e-14	1000
16	965.7786		$^2P_{3/2} 4p[^1/2]_1$	6	8.893e-14	1000

Table 3.1: Data used to convert the measured lines to population densities relating to the available models. One model for the Ar I levels, and one for the Ar II levels. Δt is the integration time used for each line. Wavelengths marked with * are average of two lines.

The last step of processing of the raw data is to define a single excited macro-state for both neutral and singly ionized Argon. This is done by using the statistical weights of the individual model levels to find an average density which could be divided back into the model's level densities. In this way there is a single effective excited state density used for each ion in eq. 3.5, where $N=4$ for Ar I and $N=3$ for Ar II. For the example spectrum above, this results in excited macro-state densities for Ar I and Ar II of $n_{ArI}^* = 2.6E12 \text{ m}^{-3}$ and $n_{ArII}^* = 4.7E10 \text{ m}^{-3}$.

$$n^* = \left(\sum g_k \right) \frac{1}{N} \sum n_k / g_k \quad (3.5)$$

Ion	Model #	g_k
Ar I	6	3
Ar I	7	20
Ar I	8	8
Ar I	9	3
Ar II	13	12
Ar II	14	20
Ar II	15	10

Table 3.2: Statistical weights used for each modeled level.

Chapter 4: Using Argon Models to find n_e and T_e

Models are employed to relate spectral emission measurements to the properties of the plasma being observed. A method of measuring the density of an excited state was shown in chapter two. In order to use that information, a model is needed that determines the excited state density in terms of the ground state density and the electron density and temperature which would give a relation between all of those quantities.

4.1 INTRODUCING ATOMIC PROCESSES

Each electron bound within an atom has a unique set of quantum numbers that defines the state of that electron within the atom. The atom is considered in the ground state when all of the electrons bound to the atom fill the lowest possible energy states. For the models needed for this work, an excited atom is one that has one of the electrons in highest energy level of the ground state is excited to a higher energy.

All of the atoms in their ground state defines a particular population, where the density of those atoms is denoted here as $n_1 [m^{-3}]$. All of the atoms with their outer electron in the same excited state also define a population denoted n_k , where $k = 1, 2, 3 \dots$ is the numeric label of the state the outer electron is in. A part of the notation used here is defining the total density of atoms in any state as $n_0 = \sum_k n_k$, but for practical purposes it is not much different than the ground state density $n_1 \cong n_0$, and so they may be used interchangeably. The purpose of the models employed here are then to determine the values of n_k for some finite number of the excited states.

The transitions between states can be caused by either a collision from outside the atom, or by absorbing or emitting a photon of the appropriate energy.

A downward transition can happen spontaneously by the emission of a photon with a probability of $P = 1 - e^{-\Delta t A_{ji}}$, where Δt is the time interval from when the

electron is known to be in the state j , and A_{ji} is the Einstein coefficient for the transition from state j to i which has units of s^{-1} . Therefore, on a time-scale of $\tau = 1/A_{ji}$ it becomes very likely that the spontaneous emission of a photon will happen, and the electron will go into a lower energy state.

The other dominant type of transition is induced by a collision from an external electron. The chance that an incident electron will cause a transition is determined by the collision cross section σ_{ji} . The cross section is a function of the velocity of the incident electron, so the total rate of transition causing collisions is only found by integrating the cross section over the whole velocity distribution of electrons: $n_e \langle \sigma_{ji} v \rangle = \int d\underline{v}' v' \sigma_{ji}(v') f_e(\underline{v}')$, which also has units of s^{-1} . This, of course, would require knowledge of $f(\underline{v})$.

The usual assumption is that the electron distribution is nearly Maxwellian, where $f(\underline{v}) = n_e \left(\frac{m_e}{2\pi k T_e} \right)^{3/2} \exp \left[-\frac{1}{2} m_e v^2 / k T_e \right]$. Given the temperature of the plasma, this will determine the velocity integrated collision rate, assuming also that the cross section is known.

4.2 CORONAL AND LTE MODELS

A common starting point for discussing modeling of excited state populations is to consider two extremes in electron density. The two extremes are defined by comparing the rate of the spontaneous radiative transitions to the rate at which electron collisions induce transitions. Radiative transition rates are encoded in the Einstein coefficients A_{ji} , and depend on which level is being considered but not the plasma conditions. Collision rates with electrons depend on the velocity integrated collision rate for the transition, $n_e \langle \sigma_{ji} v \rangle$, and so depend both on the level and the plasma conditions.

If the plasma is of sufficiently low density, then $A_{ji} \gg n_e \langle \sigma_{ji} v \rangle$ and the transitions are dominated by the radiative process. Excitations from other excited levels can usually be neglected for this reason, since they will typically spontaneously decay to a lower energy state before a collision can excite it to a higher level. The only non-radiative process that is needed is the excitation from the ground state. This leads to a very simple model if excitations from the ground state to a level is balanced by radiative transitions out of the level: $n_1 n_e \langle \sigma_{1k} v \rangle - A_k n_k = 0$, where $A_k = \sum_i A_{ki}$ is the total rate of spontaneous emissions.

If the plasma is of sufficiently high density, on the other hand, then $A_{ji} \ll n_e \langle \sigma_{ji} v \rangle$ and the transitions are dominated by collisions with electrons. If it is then also assumed that the electrons are near thermal equilibrium, and the atomic levels are also in near thermal equilibrium with the electrons, then the populations are determined completely by statistical mechanics. This condition is called local thermal equilibrium, or LTE. The only atomic data needed is the excitation energies of the levels of interest to use the Boltzmann distribution for the levels: $\frac{n_k}{n_i} = \frac{g_k}{g_i} \exp[-(E_k - E_i)/kT_e]$. The other consequence of LTE is that each collisional process must be balanced by its inverse process, called detailed balance, which puts a restriction on the collision cross sections used. When the system approaches LTE it must be true that $n_k \langle \sigma_{ki} v \rangle = n_i \langle \sigma_{ik} v \rangle$, or substituting in the above relation $\frac{\langle \sigma_{ik} v \rangle}{\langle \sigma_{ki} v \rangle} = \frac{g_k}{g_i} \exp[-(E_k - E_i)/kT_e]$.

Using the atomic data for neutral Argon used in the model by Bogaerts et. al. ^[4], the relative importance of radiative versus collisional transitions, $\frac{A_k}{A_k + n_e \sum_i \langle \sigma_{ki} v \rangle}$, can be calculated for each level as in figure 4.1. For the collision terms, a range of values for n_e and T_e are used that are typical to the Helimak. Levels with this ratio closer 1 are determined mostly by radiative processes, such as those of lower level numbers. Those with the ratio toward 0 are determined mostly by collisions.

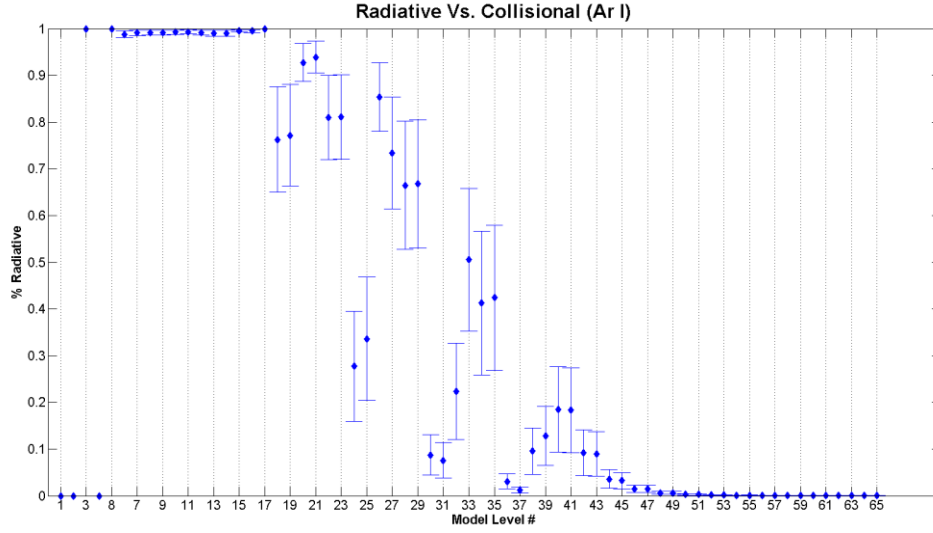


Figure 4.1: $\frac{A_k}{A_k + n_e \sum_i \langle \sigma_{ki} v \rangle}$ calculated for each level in the Bogaerts model^[4]. Values of n_e and T_e used are typical of the Helimak.

As can be seen, the ground state, $k=1$, as well as two other lower levels, $k=2$ & 4 , have a ratio of identically 0. The levels 2 and 4 are called meta-stable levels because, similar to the ground state, they have no dipole allowed radiative transition. Otherwise, the lower levels are mostly determined by radiative transitions. The higher levels become more dominated by collisions until at some point they are completely collisional. This mix of dependence on both radiative and collisional processes is what motivates a more complex model.

4.3 COLLISIONAL-RADIATIVE MODEL

The idea behind a collisional radiative model is to construct a rate equation for each population that would be valid in any density regime. Each could have any number of terms, each representing some atomic physics process, but can generally be grouped into gain and loss rates that are functions of the populations and the plasma conditions as in equation (4.1). Solving for a steady-state, $\frac{dn_k}{dt} = 0$, then gives the values of n_k . This

will result in a number of coupled equations, one for each level, which must be solved simultaneously.

$$\frac{dn_k}{dt} = R_k^{gain}(n_{i \neq k}, n_e, T_e, \dots) - R_k^{loss}(n_i, n_e, T_e, \dots) \quad (7.1)$$

If the plasma conditions are not uniform, then the population densities will necessarily not be uniform either. In principle the rate equations would be non-local to account for transport of the excited atoms. However, because transition rates are so high compared to the thermal velocities and characteristic length scale of the plasma, $\frac{R_k^{loss}}{n_k} \gg \frac{v_{th}}{L}$, the streaming terms can usually be neglected. Figure 4.2 shows typical level lifetimes for argon levels. A transit time for an Argon atom would be $\frac{L}{v_{th}} \cong 3ms$, and so with the exception of the ground state, and possibly the meta-stable states, all other levels will not depend on non-local effects.

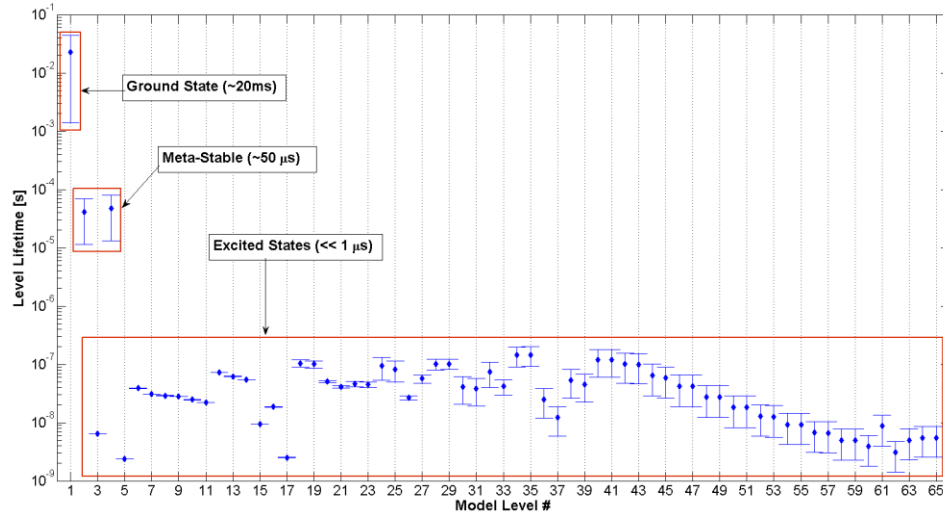


Figure 4.2: Level lifetimes calculated for each level in the Bogaerts model^[4]. Values of n_e and T_e used are typical of the Helimak.

Determining the ground state density is the subject of chapter 5, and so it will be assumed here that it is already known. The meta-stable levels could potentially cause problems because their rates could depend more on non-local streaming than the excited states, but the streaming time scale is still much longer than the level lifetime and so their non-local effects will not be dealt with.

4.4 ARGON ICR MODEL

The collisional-radiative model used for neutral Argon was taken from the work of Bogaerts et. al.^[4], derived from Vlček's original work^{[10][11]}. It includes 65 effective levels including the ground state and 2 meta-stable levels. Each effective level is a grouping of two or more physical levels of similar energy, and are added together using the sub-level's statistical weights, such that the sub-level densities are written in terms of the effective level density as $n_j = \frac{g_j}{g_k} n_k$, where $g_k = \sum_j g_j$. The energy levels of the effective levels are shown in figure 4.3.

The levels are divided into two groups, relating to whether the excited electron was in the spin up or spin down state, leaving the core electron configuration with either $j_c = 3/2$ or $j_c = 1/2$. This causes splitting of all the excited level energies into the two groups. All of the levels that give rise to measured lines in the visible spectrum are 4p to 4s transitions from both groups, coming from the effective levels 6 through 11.

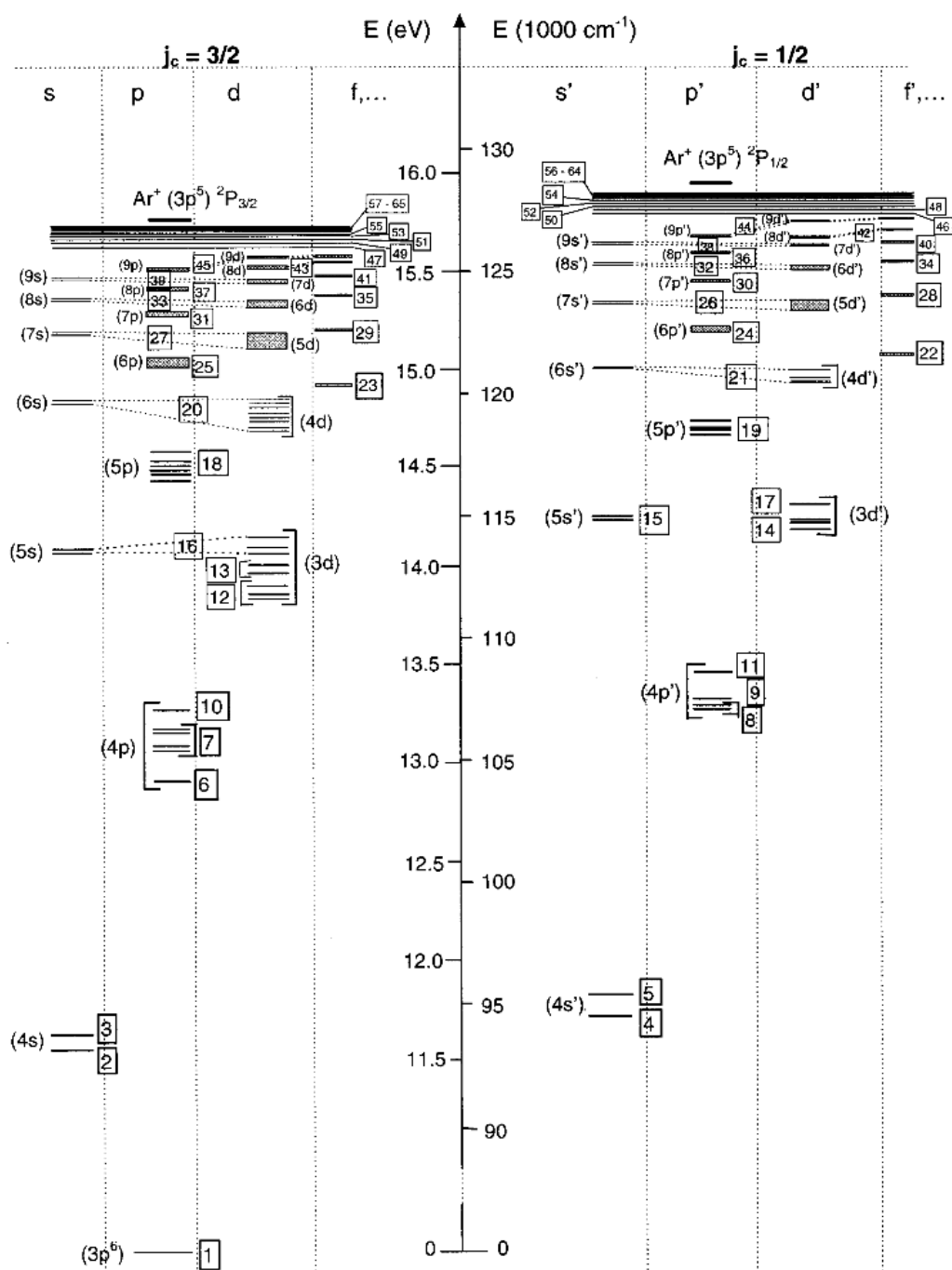


Figure 4.3: Energy level diagram of Ar I effective levels taken from Bogaerts^[4].

The processes kept from the model are electron impact excitation, de-excitation, ionization, three-body and radiative recombination, and radiative decay. The neutral gas is of sufficiently low pressure that neutral collisions are infrequent and so the atom-atom terms from the model are not included. The gas is also optically thin and so the escape factor from the model is set to unity. The resulting rate equation is then equation 4.2.

Because the effective levels are not numbered in order of increasing excitation energy, E_k^{exc} , the notation unfortunately becomes somewhat unconventional. A convention is adopted that a rate coefficient is zero for un-allowed transitions. For example, the excitation coefficients $K_{ik}^{exc.}$ are zero by definition when $E_k < E_i$. This allows the indices to be summed over all levels. This makes it appear as though excitations, de-excitations, and radiative decay exists between all levels, but this is not really the case.

$$\begin{aligned} \frac{dn_k}{dt} = & \sum_{i=1}^N n_i [K_{ik}^{exc.} + K_{ik}^{de-exc.} + A_{ik}] + n^{Ar^{+1}} (K_k^{RR} + K_k^{3BR}) \\ & - n_k \left[K_k^{ion} + \sum_{i=1}^N [K_{ki}^{exc.} + K_{ki}^{de-exc.} + A_{ki}] \right] \\ = & 0 \end{aligned} \quad (7.2)$$

The ground state was not modeled as this will be determined later. These N-1 coupled equations are solved by iteration as coded in the Matlab routines from the work of E. Sciamma^[5], with the initial solution having $n_{k>1} = 0$.

To relate these solutions to the measured excited states of neutral Argon in chapter 3, the solutions to levels 6 through 9 are grouped together into a single macro-state in the same way that was done with the spectroscopic measurements using eq. 3.5. The solutions n_k/n_1 were then tabulated for a range of electron temperatures and densities in table 4.1.

	1E16	2E16	5E16	1E17	2E17	5E17	1E18	2E18
0.5	4.742E-11	1.520E-10	7.450E-10	2.605E-09	9.516E-09	5.630E-08	2.287E-07	9.912E-07
1	4.455E-11	1.254E-10	5.365E-10	1.705E-09	5.605E-09	2.783E-08	9.504E-08	3.275E-07
2	1.396E-08	2.785E-08	6.890E-08	1.354E-07	2.614E-07	5.914E-07	1.022E-06	1.612E-06
5	8.228E-07	1.636E-06	4.013E-06	7.769E-06	1.460E-05	3.079E-05	4.849E-05	6.703E-05
10	2.916E-06	5.802E-06	1.423E-05	2.752E-05	5.154E-05	1.079E-04	1.687E-04	2.315E-04
20	4.956E-06	9.881E-06	2.432E-05	4.720E-05	8.890E-05	1.885E-04	2.993E-04	4.196E-04

Table 4.1: Solutions from Ar I effective levels 6 through 9 combined into macro-state, divided by ground state density to give the relative density. Each row is electron temperature range in eV. Each column is the electron density range in m^{-3} . Values are found by multiplying by the ground state density.

4.5 ARGON II CR MODEL

The model for Ar II comes from ADAS, the Atomic Data Analysis Structure. As described by Ella Sciamma^[4] the model used was similar in structure to that of the Ar I model with the use of 35 effective levels. Tables for three of those levels were generated originally by Dr. W. L. Rowan, and are taken from Ella's work. The changes are that the original tables were tabulated as a relative density such that the excited state density was found by multiplying by the ion density, as in the Ar I table 4.1.

Because there is very little double ionization, the ion density should be very close to the electron density $n_{ArII} \cong n_e$. The table entries were multiplied by the corresponding electron density to give the absolute density of the excited states. Also, the three Ar II level tables were combined in the same way as table 4.1 for Ar I using eq. 3.5, resulting in table 4.2.

	1E16	2E16	5E16	1E17	2E17	5E17	1E18	2E18
0.5	8.521E-07	3.815E-06	3.120E-05	1.692E-04	9.867E-04	1.054E-02	6.203E-02	3.555E-01
1	1.982E+02	8.404E+02	6.045E+03	2.892E+04	1.464E+05	1.324E+06	7.161E+06	3.899E+07
2	2.695E+06	1.109E+07	7.473E+07	3.288E+08	1.511E+09	1.192E+10	5.927E+10	3.042E+11
5	6.250E+08	2.540E+09	1.653E+10	6.956E+10	3.002E+11	2.163E+12	1.007E+13	4.934E+13
10	3.013E+09	1.216E+10	7.827E+10	3.258E+11	1.379E+12	9.647E+12	4.382E+13	2.107E+14
20	4.988E+09	2.014E+10	1.286E+11	5.319E+11	2.229E+12	1.537E+13	6.869E+13	3.256E+14

Table 4.2: Solutions from Ar II effective levels 13 through 15 combined into macro-state, in units of m^{-3} . Each row is electron temperature range in eV. Each column is the electron density range in m^{-3} .

4.6 DETERMINING n_e AND T_e

The two tables constructed from the collisional radiative models represent two functions of n_e and T_e : $\frac{n_{ArI}^*}{n_{ArI}} = C(n_e, T_e)$, and $n_{ArII}^* = D(n_e, T_e)$, where n^* is the excited state density. If both values of $\frac{n_{ArI}^*}{n_{ArI}}$ and n_{ArII}^* are measured as in chapter 3, then n_e and T_e are found by solving equations (4.3) and (4.4) simultaneously. For practical reasons the solution was found in the log scale of the densities since it covers many orders of magnitude.

$$f_I(\log(n_e), T_e) = \log\left(\frac{n_{ArI}^*}{n_{ArI}}\right) - \log(C(n_e, T_e)) = 0 \quad (7.3)$$

$$f_{II}(\log(n_e), T_e) = \log(n_{ArII}^*) - \log(D(n_e, T_e)) = 0 \quad (7.4)$$

These functions are discrete because the tables were only calculated for certain values, so the functions were also interpolated using the Matlab interp2 function, with the cubic interpolation method. An example solution is plotted in figure 4.4 using the

example measurement calculation from chapter 3: $n_{ArI} = 3.1E17 m^{-3}$, $n_{ArI}^* = 2.6E12 m^{-3}$, and $n_{ArII}^* = 4.7E10 m^{-3}$.

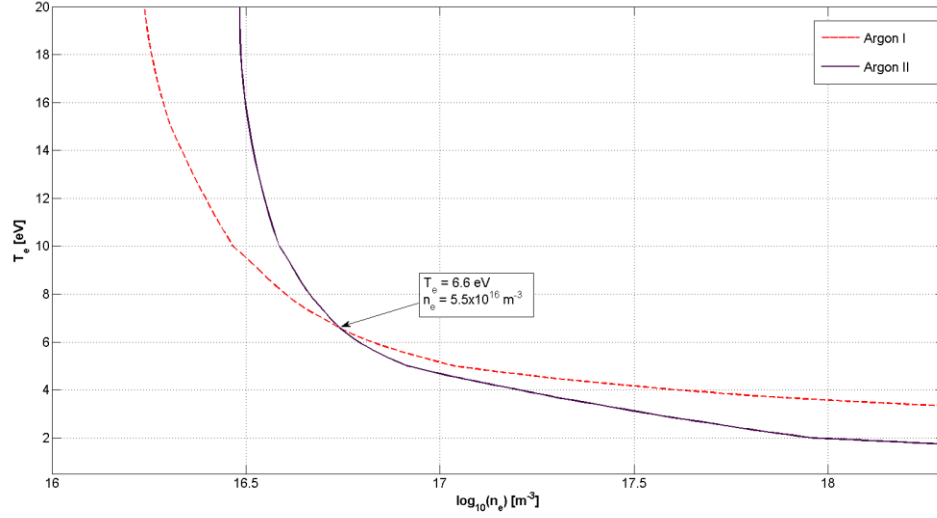


Figure 4.4: Solution of equations 4.3 and 4.4. The intersection of the two curves gives the value of n_e and T_e .

Solving equations 4.3 and 4.4 produce two curves that are now only functions of one or the other variable. The intersection of the two curves will give the unique values that are consistent with the spectroscopic measurements and the collisional-radiative models. In this example, the values determined graphically are $n_e = 5.5E16 m^{-3}$ and $T_e = 6.6 \text{ eV}$.

Matlab code was written to solve for the intersection point programmatically. The functions are still discrete on a grid. The first step was to check each square of the grid to see if one of the functions had a zero in that square. Given the value of the function on the four grid points, $f_{00}, f_{01}, f_{10}, f_{11}$, if two point on the same side alternate from positive to negative, then the zero curve must pass between the two points. The intersection of the curve and that side of the square is found using linear interpolation

between the two values. The curve must intersect two sides of the square, and so the other intersection point is also found.

When a square is found that the first function has a zero inside, then the other function was checked to see if it had a zero in the same square. If both functions have zeros in the square then the code checked to see if the two zero curves intersected by using linear interpolation again given the two intersection points of each curve using eq. 4.5 and 4.6. Here the curves are denoted by a and b.

$$x_{intersect} = \frac{x_2^b(x_2^a(y_1^a - y_1^b) + x_1^a(y_1^b - y_2^a)) + x_1^b(x_1^a(y_2^a - y_2^b) + x_2^a(y_2^b - y_1^a))}{(x_2^b - x_1^b)(y_1^a - y_2^a) + (x_1^a - x_2^a)(y_1^b - y_2^b)} \quad (7.5)$$

$$y_{intersect} = y_1^a + \frac{y_2^a - y_1^a}{x_2^a - x_1^a}(x_{intersect} - x_1^a) \quad (7.6)$$

4.7 FIRST CORRECTION FOR NEUTRAL DENSITY

The value for the neutral density used above is derived from the pressure reading from before the shot. If it is assumed that the total number of atoms within the vacuum chamber remains nearly constant throughout the shot, then when some fraction of them becomes ionized there are slightly less as neutrals. The total number can be expressed as the number density times the total volume of the vacuum chamber $N_0 = n_0 V_{vacuum}$, where n_0 is derived from the ion gauge pressure reading before the shot. The total number of ionized atoms would be $N_{ArII} = \langle n_{ArII} \rangle V_{plasma}$, where $\langle n_{ArII} \rangle$ is the average ion density of the plasma, and V_{plasma} is the volume of just the plasma. The number of neutrals left should then be $N_{ArI} = \langle n_{ArI} \rangle V_{vacuum} = N_0 - N_{ArII}$. Solving for the average neutral density gives equation 4.7.

$$\langle n_{ArI} \rangle = n_0 - \langle n_{ArII} \rangle \frac{V_{plasma}}{V_{vacuum}} \quad (7.7)$$

The average ion density was determined by taking a sample profile for n_e from probe measurements and computing what the average density, weighted by the absolute radial distance, in terms of the maximum value of n_e . The value determined was $\langle n_e \rangle = 0.45 \times \max(n_e)$. A value close to 0.5 was expected due to the peaked nature of the profile. The average ion density then can use the same value since the plasma should only be singly ionized. The maximum value of n_e can already be determined by the above method.

The volume of the plasma is somewhat less than the vacuum chamber since the plasma does not extend all the way to the top or bottom. The termination plates extend approximately 28cm from the top and bottom, but the plasma does not end abruptly. With the chamber being 2m in height, an effective plasma height of 1.72m is used, giving a volume ratio of $\frac{V_{plasma}}{V_{vacuum}} = 0.86$.

Using this above to correct for the neutral density changes the solution, including the value of maximum n_e . So the process must be iterative to converge to a self-consistent value. Continuing with the example calculations, this process changes the above solution values to $n_e = 5E16 \text{ m}^{-3}$ and $T_e = 7.2 \text{ eV}$, with the neutral density reduced to $\langle n_{ArI} \rangle = 0.935 \times n_0$.

Chapter 5: Neutral Density Profile

The question of what the neutral density profile is for Argon within the Helimak will try to be addressed theoretically here.

5.1 MOTIVATION

Ionization rate data is available from the Bogaerts^[4] CR model used in calculating density and temperature, but another source of Argon ionization rates is referenced from Arnaud et al^[12]. The velocity integrated cross section $\langle \sigma_{ion} v \rangle$ is plotted in figure 5.1 from both sources for neutral Argon, as well as the first two ionization states.

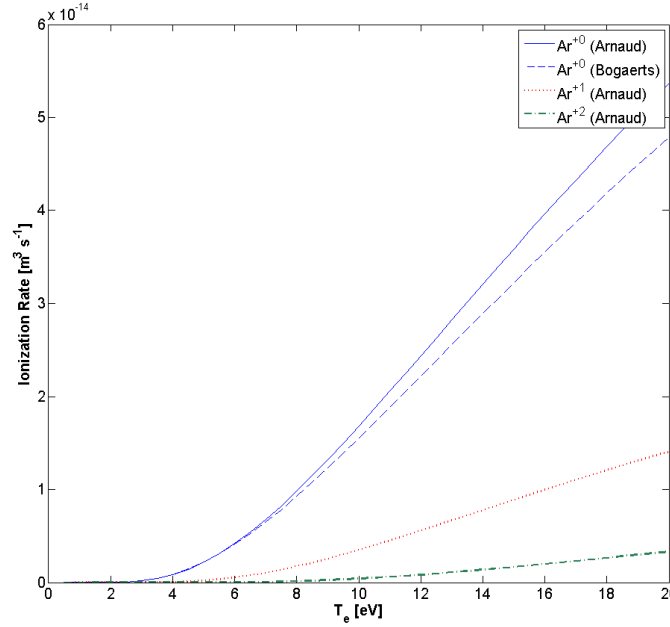


Figure 5.1: Ionization rates for Argon from Bogaerts^[4] and Arnaud^[12].

The ionization rate for neutral Argon at $T_e = 10\text{eV}$ and $n_e = 5E16\text{ m}^{-3}$ is about $K_{ion} = n_e \langle \sigma_{ion} v \rangle = 800\text{ s}^{-1}$. Using $v_{th} = 340\text{ m/s}$ ($T=300\text{K}$) gives a mean free path of an atom before being ionized of $\lambda_{ion} = \frac{v_{th}}{K_{ion}} = 0.4\text{ m}$. The Helimak's scale is of 1m, which

implies that a significant fraction of the neutral atoms could be ionized while traversing the Helimak chamber. That is, it would be hard to justify that the profile must be flat.

The ionization rate would be a peaked profile since the electron density and temperature also have peaked profiles. Also, since the neutral atoms velocities should be close to thermal distribution, the mean free path would depend on exactly what velocity each atom is traveling. To find the actual profile of the neutral density, the non-local and thermal effects should be included.

The neutral-neutral collisional mean free path as defined by $\lambda_{00} = \frac{1}{n_0 \sigma_{00}} \cong 10m$, with $\sigma_{00} = 36 \text{ \AA}^2$ for Argon [ref. ??], which is larger than the dimension of the Helimak chamber. The gas is in the molecular flow, or ballistic, regime where collisions with the walls are more frequent than with other atoms.

5.2 KINETIC MODEL

A kinetic model is used to solve for the neutral density. Even though this approach is computationally intensive, it is straightforward. The evolution of the gas can be described by the Boltzmann equation, (5.1), which models the distribution of particles in velocity and spatial dimensions $f(\bar{x}, \bar{v}, t)$. For three spatial dimensions, the distribution function has six dimensions plus time.

$$\frac{\partial f}{\partial t} + \bar{\nabla}_x \cdot (f \bar{v}) + \bar{\nabla}_v \cdot (f \bar{a}) = \frac{\partial f}{\partial t_{coll}} + s \quad (12.1)$$

The first term on the left hand side, $\frac{\partial f}{\partial t}$, is simply the time rate of change of the distribution at a particular velocity, position, and time. The second term, $\bar{\nabla}_x \cdot (f \bar{v})$, represents the streaming of particles through space. The third term, $\bar{\nabla}_v \cdot (f \bar{a})$, represents how forces move the particles through velocity space. The acceleration vector can also be a function of both position and velocity $\bar{a}(\bar{x}, \bar{v}, t)$. The first term on the RHS, $\frac{\partial f}{\partial t_{coll}}$, is the effect of collisions between particles in the distribution as well as other species of particles, and also moves particles around in velocity space. This term can be complicated and would in reality be a functional of the distribution itself. The last term, $s(\bar{x}, \bar{v}, t)$, is the source term which can add or remove particles, such as through ionization and recombination.

A neutral gas does not produce nor interact with electromagnetic fields. The interaction with the gravitational force can also of course be neglected since $\frac{3}{2}kT \gg mgh$. This allows the dropping of the external forces altogether. Since the neutral collision rate is very low, the collision term will also be dropped. Since a steady state solution is desired this leaves eq. 5.2. The source term within the plasma will only be due to ionization. Recombination is much slower within the plasma by over an order of magnitude and so will be dropped. This leaves $s = -f K(n_e, T_e)$. The source term will need to include recombination at the wall somewhere, but will be dealt with separately.

$$\bar{\nabla}_x \cdot (f \bar{v}) = -f K(n_e, T_e) \quad (12.2)$$

If a particular direction is chosen, $v \frac{\partial}{\partial l} \equiv \bar{v} \cdot \bar{\nabla}_x$, then the equation can be rearranged into eq. 5.3. The ionization rate can also be written as a function of position since the electron density and temperature are functions of position. This equation can be directly integrated in the form of eq. 5.4 if the position is also parameterized in terms of l to give eq. 5.5, where $L(r, z, \hat{r} \cdot \hat{v}, \hat{z} \cdot \hat{v})$ is the distance to the wall from the test position along the direction $-\hat{v}$.

$$v \frac{\partial f}{\partial l} = -fK(\bar{x}) \quad (12.3)$$

$$\frac{1}{f} df = -\frac{1}{v} K(\bar{x}'(l)) dl \quad (12.4)$$

$$f(\bar{x}, \bar{v}) = f(\bar{x}_0, \bar{v}) \exp \left[-\frac{1}{v} \int_0^L dl K(\bar{x}_0 + l\hat{v}) \right] \quad (12.5)$$

The position the path intersects the wall is $\bar{x}_0 \equiv \bar{x} - L\hat{v}$. The electron density and temperature are assumed to be cylindrically symmetric, so the rate K should only depend on the radial coordinate. The radius can be parameterized in terms of l to give eq. 5.6. Using spherical coordinates for the velocity, and $\hat{r} \cdot \hat{v} \equiv \sin \varphi \cos \theta$ and $\hat{z} \cdot \hat{v} \equiv \cos \varphi$ at the point where the solution is being computed.

$$r' = [(r + (l - L) \sin \varphi \cos \theta)^2 + (l - L)^2 \sin^2 \varphi \cos^2 \theta]^{1/2} \quad (12.6)$$

The next task is to define the function L , which depends on the geometry of the Helimak. The path can be broken into two components, one perpendicular to the z -axis and one parallel. If the floor and ceiling of the Helimak are ignored for a moment, the perpendicular component has only two possible cases. One where the path originates

from the outer wall, and one from the inner wall, depending on the value of θ , which are depicted in figure 5.2.

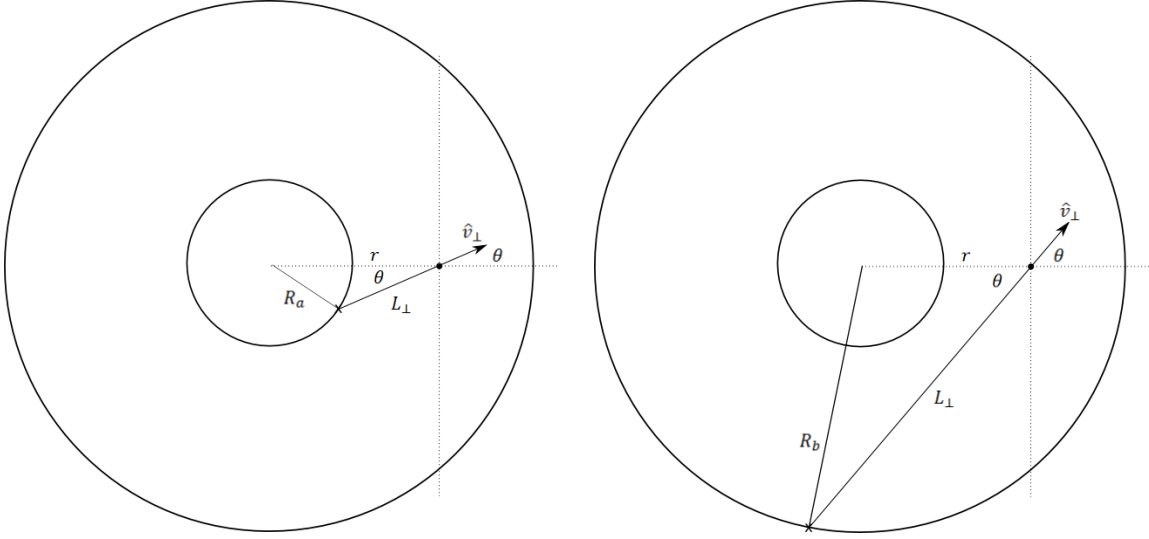


Figure 5.2: Component of path perpendicular to z-axis of Helimak. Can intersect either inner wall or outer wall depending on θ . (a) [left] Path Intersects Inner Wall. (b) [right] Path Intersects Outer Wall.

The law of cosines can be used to derive the expressions for L_{\perp} . For the inner wall this gives $R_a^2 = r^2 + L_{\perp}^2 - 2rL_{\perp} \cos \theta$, and for the outer wall $R_b^2 = r^2 + L_{\perp}^2 - 2rL_{\perp} \cos \theta$, which can be solved using the quadratic formula. At the transition point the path is tangent to the inner wall giving $\sin \theta_t = \frac{R_a}{r}$. When $\theta \leq \theta_t$ the inner wall value is used, and when $\theta > \theta_t$ the outer wall is used giving eq. 5.7.

$$L_{\perp} = r \cos \theta + \begin{cases} -\sqrt{R_a^2 - r^2 \sin^2 \theta}, & \theta \leq \theta_t \\ \sqrt{R_b^2 - r^2 \sin^2 \theta}, & \theta > \theta_t \end{cases} \quad (12.7)$$

The parallel component is simply the distance to either the floor or the ceiling. However, there are additional restrictions now to match both the wall and the floor and ceiling conditions depending on φ depicted in figure 5.3. The solution is summarized in eq. 5.9.

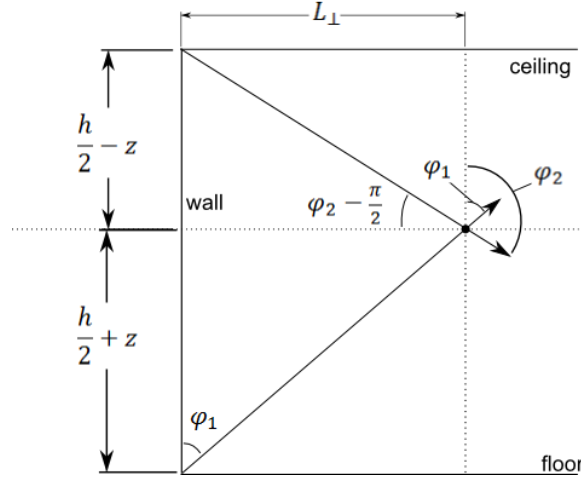


Figure 5.3: Matching wall condition with floor and ceiling.

$$\begin{aligned}\varphi_1 &= \tan^{-1} \left(\frac{L_{\perp}}{\left(\frac{h}{2}+z\right)} \right) \\ \varphi_2 &= \tan^{-1} \left(\frac{\left(\frac{h}{2}-z\right)}{L_{\perp}} \right) + \frac{\pi}{2}\end{aligned}\tag{12.8}$$

$$L = \begin{cases} \left(\frac{h}{2}+z\right) \sec \varphi, & 0 \leq \varphi \leq \varphi_1 \\ L_{\perp} \csc \varphi, & \varphi_1 < \varphi < \varphi_2 \\ \left(\frac{h}{2}-z\right) (-\sec \varphi), & \varphi_2 \leq \varphi \leq \pi \end{cases}\tag{12.9}$$

The solution in eq. 5.5 still depends on the value of the distribution at the boundary $f(\bar{x}_0, \bar{v})$. The boundary condition is that the total flux at the walls, minus the source, must be zero. The total particle flux is the first velocity moment of the

distribution. For velocities going into the wall, the distribution is found using eq. 5.5, where $f(\bar{x}_0, \bar{v})$ is the value at some other wall coming inward. The distribution coming from the wall must be found to match the boundary condition.

To simplify the process of solving the boundary condition, it will be assumed that the part of the distribution not determined by 5.5 is Maxwellian in shape. The justification for this is that particles will scatter off the walls changing their direction and energy, and would eventually come into thermal equilibrium with the walls anyway after scattering many times.

The distribution is divided into two components with n^- and $\bar{\Gamma}^-$ defined as the particle density and flux from the part of the distribution from 5.5 going into the wall, and n^+ and $\bar{\Gamma}^+$ from the rest of the distribution that is Maxwellian like. The total density and flux at the wall is then $n = n^- + n^+$ and $\bar{\Gamma} = \bar{\Gamma}^- + \bar{\Gamma}^+$. For the walls the condition is $\hat{q} \cdot \bar{\Gamma} = 0$, where \hat{q} is the inward directed normal vector of the wall surface. The corners between the floor or ceiling and the inner or outer wall must satisfy both surface conditions.

For the flat surfaces, $\hat{q} \cdot \bar{\Gamma}^+$ is found by integrating over the half Maxwellian distribution, and results in eq. 5.11. The corners are trickier because in order to satisfy two conditions simultaneously, the distribution must have two free parameters. In the corner $\bar{\Gamma}^-$ is only defined for one quarter of the directions, so the other three quarter directions are Maxwellian like, but cannot be isotropic. If n^+ is defined in the corner as in

eq 5.10, and assuming that $\hat{q}_1 \cdot \hat{q}_2 = 0$, then the positive flux in the two directions is

found from eq. 5.12 and 5.13. $v_{th} = \sqrt{\frac{2 kT}{m}}$.

$$n^+ = \begin{cases} n_2^+, & \hat{q}_1 \cdot \hat{v} < 0, \hat{q}_2 \cdot \hat{v} > 0 \\ n_1^+ \epsilon_1 + n_2^+ \epsilon_2, & \hat{q}_1 \cdot \hat{v} > 0, \hat{q}_2 \cdot \hat{v} > 0 \\ n_1^+, & \hat{q}_1 \cdot \hat{v} > 0, \hat{q}_2 \cdot \hat{v} < 0 \end{cases} \quad (12.10)$$

$$\text{where } \epsilon_1 = \frac{(\hat{q}_1 \cdot \hat{v})^2}{(\hat{q}_1 \cdot \hat{v})^2 + (\hat{q}_2 \cdot \hat{v})^2}, \text{ and } \epsilon_2 = \frac{(\hat{q}_2 \cdot \hat{v})^2}{(\hat{q}_1 \cdot \hat{v})^2 + (\hat{q}_2 \cdot \hat{v})^2}$$

$$\hat{q} \cdot \bar{\Gamma}^+ = \frac{v_{th}}{\sqrt{\pi}} n^+ \quad (12.11)$$

$$\hat{q}_1 \cdot \bar{\Gamma}^+ = \frac{v_{th}}{6\sqrt{\pi}} (5n_1^+ - 2n_2^+) \quad (12.12)$$

$$\hat{q}_2 \cdot \bar{\Gamma}^+ = \frac{v_{th}}{6\sqrt{\pi}} (5n_2^+ - 2n_1^+) \quad (12.13)$$

$$\hat{q} \cdot \bar{\Gamma}^- = \int_{\hat{q} \cdot \bar{v} < 0} d\bar{v} (\hat{q} \cdot \bar{v}) f(\bar{x}, \bar{v}) \quad (12.14)$$

The boundary is then discretized, and coefficients computed to give the contribution of each boundary element to the outward particle flux at every other boundary element using eq. 5.5, and eq. 5.14. The outward flux at each point is then found by summing over all of the contributions as in eq. 5.15 for flat surfaces, and 5.16 for the corners. The addition of s_j is the source term from recombination of ions at the wall. The inward directed density at the wall can then found by solving 5.15 and 5.16 by iteration.

$$\hat{q}_i \cdot \bar{\Gamma}_i^- = \sum_{j \neq i} A_{ij} [n_j^+ + s_j] = \hat{q}_i \cdot \bar{\Gamma}_i^+ = \frac{v_{th}}{\sqrt{\pi}} n_i^+ \quad (12.15)$$

$$\sum_{j \neq i} A_{ij} [n_j^+ + s_j] = \frac{v_{th}}{6\sqrt{\pi}} (5n_i^+ - 2n_k^+) \quad (12.16)$$

Assuming a Maxwellian distribution at the boundary has another important feature. Since the inward half of the distribution can then be written as eq. 5.17, integrating 5.5 over all velocity space to get the first two moments of the distribution can be simplified by expressing the integral over the magnitude of velocity as a pre-computed function. The integral in the exponent of 5.5 can be defined as $v_K = \int_0^L dl K(\bar{x}_0 + l\hat{v})$, a characteristic velocity below which the distribution is highly attenuated. Using the dimensionless parameters $\alpha = v_K/v_{th}$ and $\beta = v/v_{th}$, the first two moments can be written as eq. 5.18 and 5.19.

$$f(\bar{x}_0, \bar{v}) = n^+(\bar{x}_0) 2(\sqrt{\pi} v_{th})^{-3} \exp[-v^2/v_{th}^2] \quad (12.17)$$

$$n(\bar{x}) = \frac{2}{\pi^{3/2}} \iint d\theta d\varphi \sin \varphi n^+(\bar{x}_0) M(\alpha) \quad (12.18)$$

$$\bar{\Gamma}(\bar{x}) = \frac{2v_{th}}{\pi^{3/2}} \iint d\theta d\varphi \sin \varphi \hat{v} n^+(\bar{x}_0) N(\alpha) \quad (12.19)$$

$$M(\alpha) = \int_0^\infty d\beta \beta^2 \exp[-\beta^2 - \alpha/\beta] \quad (12.20)$$

$$N(\alpha) = \int_0^\infty d\beta \beta^3 \exp[-\beta^2 - \alpha/\beta] \quad (12.21)$$

The two functions $M(\alpha)$ and $N(\alpha)$, plotted in figure 5.4, can be pre-computed and placed in a lookup table. The integral's over θ and φ must still be calculated at every location since n^+ and α are complicated functions of θ , φ , r and z .

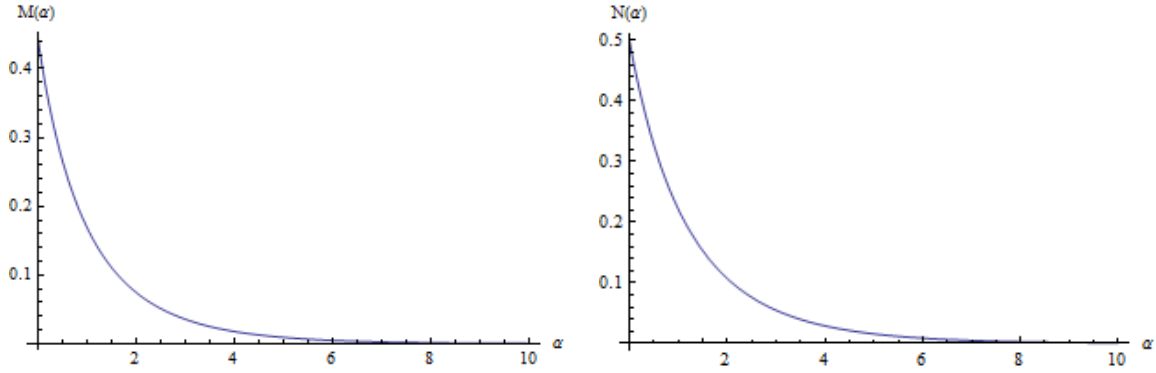


Figure 5.4: Integrals $M(\alpha)$ and $N(\alpha)$ plotted over a range of the parameter.

There are several obvious symmetries that will be used to minimize the amount of computation required. The solution will be axially symmetric, so it needs only be calculated for r and z . There is an up-down symmetry so that only the $+z$ positions need to be computed. There is also reflection symmetry in velocity space along the azimuthal direction of the Helimak, so only half of the directions need to be computed.

The integral over θ and φ must be computed numerically for a discrete set of points on the unit sphere. If the points are placed at evenly spaced increments of θ and φ , as depicted in figure 5.5, then bilinear interpolation (eq 5.22) can be used between the points.

$$\begin{aligned}
f_{ij}(\theta, \varphi) = \frac{1}{\Delta\theta\Delta\varphi} & [f(\theta_i, \varphi_j)(\theta_{i+1} - \theta)(\varphi_{j+1} - \varphi) \\
& + f(\theta_{i+1}, \varphi_j)(\theta - \theta_i)(\varphi_{j+1} - \varphi) \\
& + f(\theta_i, \varphi_{j+1})(\theta_{i+1} - \theta)(\varphi - \varphi_j) \\
& + f(\theta_{i+1}, \varphi_{j+1})(\theta - \theta_i)(\varphi - \varphi_j)]
\end{aligned} \tag{12.22}$$

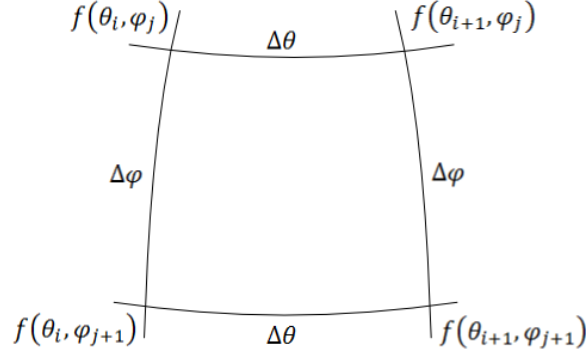


Figure 5.5: Discrete segment on the unit sphere.

The interpolated function can be integrated over its domain analytically (eq. 5.23).

All of the discrete integrals can be summed to give the total integral over the sphere. The total integral simplifies to eq. 5.24.

$$\begin{aligned}
I_{ij} &= \int_{\theta_i}^{\theta_{i+1}} d\theta \int_{\varphi_j}^{\varphi_{j+1}} d\varphi \sin \varphi f_{ij}(\theta, \varphi) \\
&= \frac{1}{2} \Delta\theta \left[\left(f(\theta_i, \varphi_j) + f(\theta_{i+1}, \varphi_j) \right) \left[\cos \varphi_j \right. \right. \\
&\quad \left. \left. - \frac{\sin \varphi_{j+1} - \sin \varphi_j}{\Delta\varphi} \right] \right. \\
&\quad \left. - \left(f(\theta_i, \varphi_{j+1}) + f(\theta_{i+1}, \varphi_{j+1}) \right) \left[\cos \varphi_{j+1} \right. \right. \\
&\quad \left. \left. - \frac{\sin \varphi_{j+1} - \sin \varphi_j}{\Delta\varphi} \right] \right]
\end{aligned} \tag{12.23}$$

$$\begin{aligned}
I = 2\pi \left(1 - \frac{\sin \Delta\varphi}{\Delta\varphi}\right) [f(\varphi = 0) + f(\varphi = \pi)] \\
+ 2 \frac{\Delta\theta}{\Delta\varphi} (1 - \cos \Delta\varphi) \sum_{j=2}^{\frac{\pi}{\Delta\varphi}} \sum_{i=1}^{\frac{2\pi}{\Delta\theta}} \sin \varphi_j f(\theta_i, \varphi_j)
\end{aligned} \tag{12.24}$$

5.3 RESULTS

For the numerical runs, each coordinate was discretized into 100 divisions for r , z , θ , and φ . Values of $R_a = 0.6m$, $R_b = 1.6m$, and $h = 2m$ were used. There is some uncertainty about h since the plasma does not extend uniformly past the bias plates, which extend about 28cm from the top and bottom of the chamber. However, as was discovered after running the simulation for several values of h , from 1.44m up to 2m, it doesn't seem to change the shape of the neutral profile very much.

The fact that the plasma terminates mostly on the bias plates, and not uniformly around the floor and ceiling, means that the assumption of axial symmetry may be invalid due to the irregular nature of the recombination profile. It may also disrupt the up-down symmetry since the plasma terminates on the opposite side of the bias plate at the top as it does on the bottom. This is probably the weakest point of the model.

A radial profile for electron density and temperature are needed to define the ionization rate function K in eq. 5.5. Also needed is the recombination source profile on the walls. For n_e and T_e , a fitting function is used to approximate their profile based on probe data. The function used is eq. 5.25, where A is the maximum value of either n_e or T_e , γ is the ratio of the value at the outer wall to the maximum value, $x = \frac{r-R_a}{R_b-R_a}$, $x_p =$

$\frac{r_p - R_a}{R_b - R_a}$ (where r_p is the location of the profile peak), and $y = \left(\frac{0.5 - x_p}{x_p^2 - x_p} \right) x^2 + \left(1 - \left(\frac{0.5 - x_p}{x_p^2 - x_p} \right) x \right)$. A value of $\gamma = 0.5$ and $r_p = 1.1m$ was used for n_e , and $\gamma = 0.4$ and $r_p = 1m$ for T_e . An example fit is shown in figure 5.6.

$$h(x) = A \left(\frac{\gamma}{2} (1 - \cos(\pi y(x))) \right) + \left(1 - \frac{\gamma}{2} \right) \sin^3(\pi y(x)) \quad (12.25)$$

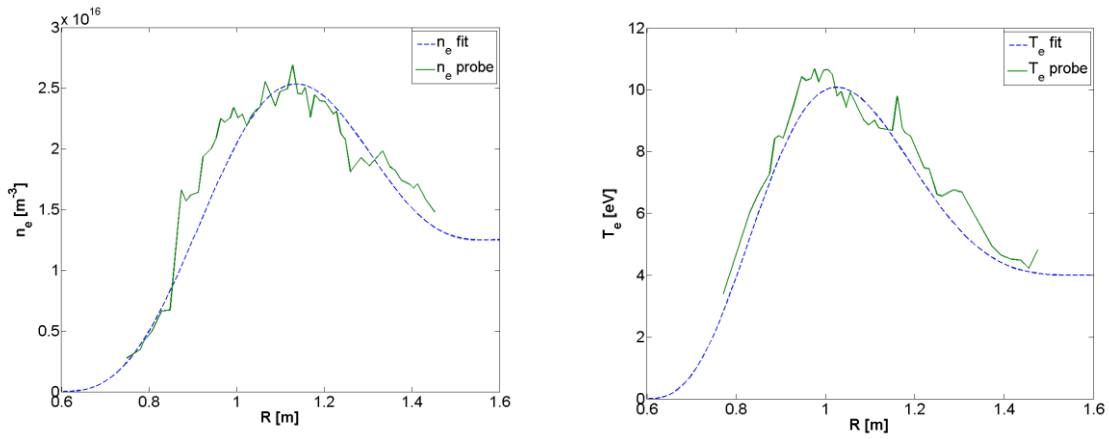


Figure 5.6: Fitting function for n_e or T_e profiles.

The recombination profile is a bit trickier to know. Ions should mostly flow vertically along field lines, which means that recombination will occur at the ceiling and floor, and not on the inner and outer walls. It will be assumed that the recombination rate is proportional to the sound speed, the electron density, and the radius: $\Gamma_{recomb} \propto C_s n_e R \propto T_e^{1/2} n_e R$. This is because the ion velocity along the field lines should scale with the sound speed, and the ion density should scale with the electron density. The pitch of the field lines also changes with radius due to the $1/R$ scaling of the toroidal field. So the vertical component of the ion velocity should scale with R . However, this only gives a

shape of the recombination profile, but not the magnitude. Given a fixed ionization rate profile, the neutral density at any point should be proportional to the recombination rate at the wall. Once the solution is computed using some arbitrary magnitude for the recombination rate, the whole solution can be re-scaled so that the average neutral density matches the measured value in eq. 4.7. Since the initial scale of the solution is then completely arbitrary, only the shape of the solution matters, it only needs to be computed in normalized units.

For an example solution, the plasma parameters used are peak values for $T_e = 10\text{eV}$ and $n_e = 5E16\text{ m}^{-3}$, and the fitting functions. The peak n_e used is higher than seen in probe data and are taken from the example calculation in chapter 4 using spectroscopic measurements.

The neutral density is plotted in figure 5.7a, which is only the upper half of the chamber, and has been normalized to the average density. The solution shows variation in the density in both r and z . The spectroscopic measurements are a chord integral through the z -direction, and so what is important is the average density along each vertical chord, which is plotted in fig 5.7b. A profile like this could be used now to make the next correction to the spectroscopically measured values of n_e and T_e in chapter 4.

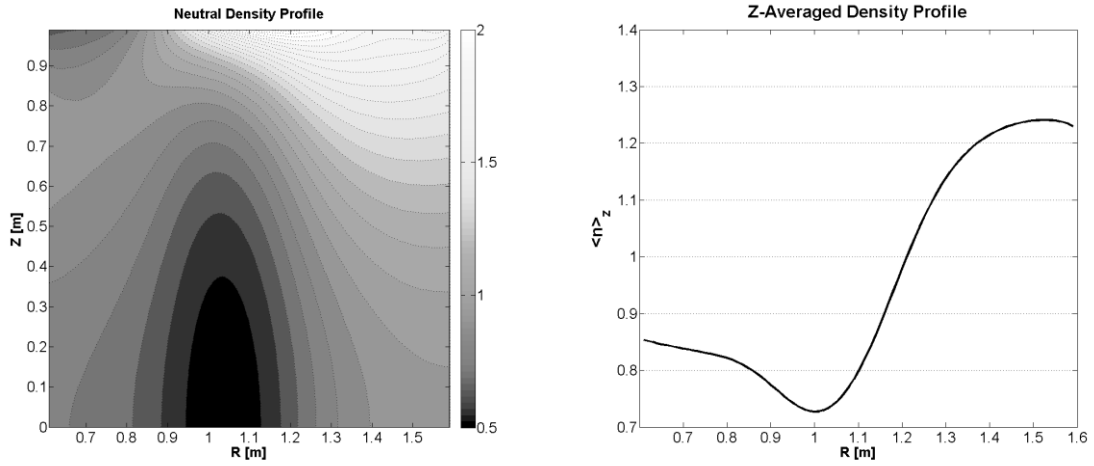


Figure 5.7 The first moment of $f(\bar{x}, \bar{v})$ plotted in upper half of Helimak chamber. (a) [left] $n(\bar{x})$, normalized to average density. (b) [right] z-average of normalized $n(\bar{x})$.

Also plotted in figure 5.8a is a streamline plot of the neutral flux density, which is the second moment of the distribution. The neutrals originate at the top and bottom from recombination, and on average flow into the region of highest ionization. This is only an average process since the individual atoms are simply bouncing from wall to wall until they are ionized. The peak averaged speed of the neutrals is around 150m/s near the top and bottom.

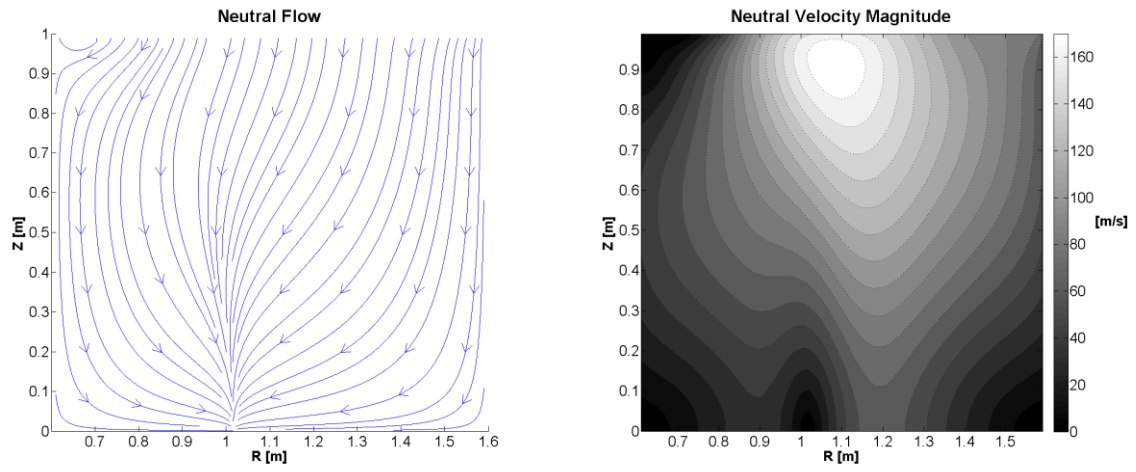


Figure 5.8 The second moment of $f(\bar{x}, \bar{v})$ in the upper half of chamber. (a) [left] streamlines of flux density $\bar{\Gamma}(\bar{x})$. (b) [right] magnitude of $v = |\bar{\Gamma}(\bar{x})/n(\bar{x})|$.

Chapter 6: Electron Velocity Distribution

6.1 MOTIVATION

In chapter 4, two atomic models were used to estimate the electron density and temperature. These models depend on the excitation cross sections for each transition, which is averaged over the velocity distribution of the electrons. It was assumed that the distribution was Maxwellian for a given temperature. However, the inelastic collisions that lead to excitation and ionization will change the electron distribution by taking energy away.

Electrons in the plasma are created through ionization of neutrals. The energy of the electrons initially comes from RF power heating some electrons, which then collide with other electrons heating them up as well. The exact electron distribution would have to satisfy the full Boltzmann kinetic equation, which would be non-local and anisotropic. Solving the exact distribution would essentially entail a full simulation of the plasma. The ultimate goal is to see how much the excitation and ionization rates change due to a deviation from pure Maxwellian distribution caused only by those collisions.

To simplify the solution, several assumptions were made. The first is that the distribution found is local with a specified effective temperature such that the average kinetic energy is $\frac{3}{2}T_e$ since the collision rates are tabulated in terms of T_e . The second is that it is isotropic, since any anisotropy makes no difference to collision rates. Energy and particle balance also have to be satisfied, and this is done by using additional operators,

which may not be entirely physical. These assumptions will hopefully still give some meaningful improvement over simply assuming a Maxwellian distribution, but a more sophisticated model could be a future improvement.

6.2 FOKKER-PLANCK SCATTERING

The starting point is the Fokker-Planck Equation, which can be used to describe the behavior of the electron distribution undergoing collisions between electrons which would drive the distribution toward a Maxwellian. The Landau-Boltzmann collision operator, denoted here as C_{ee} in eq. 6.1, is taken from The Framework of Plasma Physics^[2] in the case of electron-electron collisions. Since both populations are electrons, the notation is used so that $f(\bar{v}) = f_v$ and $f(\bar{v}') = f_{v'}$.

$$C_{ee}(\bar{v}) = \frac{\gamma_{ee}}{m_e^2} \nabla_v \cdot \int d\bar{v}' \bar{U} \cdot [f_{v'} \nabla_v f_v - f_v \nabla_{v'} f_{v'}] \quad (18.1)$$

$$\gamma_{ee} = \frac{e^4 \log \Lambda_c}{8\pi \epsilon_0^2} \quad (18.2)$$

$$\bar{U} = \frac{1}{u^3} (u^2 \bar{I} - \bar{u} \bar{u}) \quad (18.3)$$

$$\bar{u} = \bar{v} - \bar{v}' \quad (18.4)$$

$$\log \Lambda_c = 23.5 - \frac{1}{2} \log n_e + \frac{5}{4} \log T_e - \sqrt{10^{-5} + \frac{1}{16} (\log T_e - 2)^2} \quad (18.5)$$

[cm^{-3}], [eV] (taken from ^[13])

The solution desired will be isotropic, which means it only depends on the magnitude of the \bar{v} . Eq. 6.1 needs to be re-written using this condition. The velocity can be expressed as the magnitude times its unit vector $\bar{v} = v \hat{v}$. By using spherical

coordinates, and assuming only the radial derivative is non-zero, the divergence and gradient in velocity space can be written as eq. 6.6 and 6.7, and 6.1 written as 6.8.

$$\nabla_v \cdot \bar{A} = \frac{1}{v^2} \frac{\partial}{\partial v} (v^2 (\hat{v} \cdot \bar{A})) \quad (18.6)$$

$$\nabla_v a = \frac{\partial a}{\partial v} \hat{v} \quad (18.7)$$

$$C_{ee}(\bar{v}) = \frac{\gamma_{ee}}{m_e^2} \frac{1}{v^2} \frac{\partial}{\partial v} v^2 \hat{v} \cdot \int d\bar{v}' \bar{U} \cdot \left[f_{v'} \frac{\partial f_v}{\partial v} \hat{v} - f_v \frac{\partial f_{v'}}{\partial v'} \hat{v}' \right] \quad (18.8)$$

The dot products can be reduced to two expressions involving \bar{U} , which only depends on direction.

$$\hat{v} \cdot \bar{U} \cdot \hat{v} = \frac{1}{u^3} (u^2 - (\hat{v} \cdot \bar{u})^2) = \frac{1}{u^3} (u^2 - (v - v'(\hat{v} \cdot \hat{v}'))^2) \quad (18.9)$$

$$\begin{aligned} \hat{v} \cdot \bar{U} \cdot \hat{v}' &= \frac{1}{u^3} (u^2 (\hat{v} \cdot \hat{v}') - (\hat{v} \cdot \bar{u})(\hat{v}' \cdot \bar{u})) \\ &= \frac{1}{u^3} (u^2 (\hat{v} \cdot \hat{v}') \\ &\quad - (v - v'(\hat{v} \cdot \hat{v}'))(v(\hat{v} \cdot \hat{v}') - v')) \end{aligned} \quad (18.10)$$

This form lends itself to introducing the coordinates $\hat{v} \cdot \hat{v}' = \cos \varphi'$ and $\frac{v'}{v} = \beta$.

The magnitude of \bar{u} , as well as Eq. 6.19 and 6.10, can be re-written using these coordinates.

$$u^2 = v^2 (1 + \beta^2 - 2\beta \cos \varphi') \quad (18.11)$$

$$\hat{v} \cdot \bar{U} \cdot \hat{v} = \frac{\beta^2 \sin^2 \varphi'}{v(1 + \beta^2 - 2\beta \cos \varphi')^{3/2}} \quad (18.12)$$

$$\hat{v} \cdot \bar{U} \cdot \hat{v}' = \frac{\beta \sin^2 \varphi'}{v(1 + \beta^2 - 2\beta \cos \varphi')^{3/2}} \quad (18.13)$$

The distribution does not depend on the angular variables, so when the integral is performed over the angles, only the two forms involving \bar{U} are involved. Performing the integral with the expressions in 6.12 and 6.13 gives a surprisingly simple result.

$$G(\beta) = \int d\theta' d\varphi' \frac{\beta^3 \sin^3 \varphi'}{v(1 + \beta^2 - 2\beta \cos \varphi')^{3/2}} \quad (18.14)$$

$$G(\beta) = \frac{8\pi}{3} \begin{cases} \beta^3, & \beta < 1 \\ 1, & \beta \geq 1 \end{cases} \quad (18.15)$$

Plugging this back into eq. 6.8 gives the final form of the isotropic scattering operator.

$$C_{ee}(v) = \frac{\gamma_{ee}}{m_e^2} \frac{1}{v^2} \frac{\partial}{\partial v} v^2 \int d\bar{v}' G(v'/v) \left[v' f_{v'} \frac{\partial f_v}{\partial v} - v f_v \frac{\partial f_{v'}}{\partial v'} \right] \quad (18.16)$$

6.3 INELASTIC SCATTERING

To account for inelastic scattering, inelastic collision operators must be constructed for these processes. Two issues arise from this. One is that inelastic collisions do not conserve energy. The other is that if the operator is to include ionization, the creation of electrons due to that ionization will not conserve particles. This means that with no other affects included, there cannot be an equilibrium solution. Additional operators must be included to find a steady state solution to maintain the target electron density and temperature, which is defined by the average energy $\frac{3}{2}T_e = \langle \frac{1}{2}m_e v^2 \rangle$.

The inelastic operator due to excitation collisions is the simpler than for ionization, as the energy of the incident electron is reduced by a fixed amount $\Delta\epsilon$ due to an inelastic collision. It consists of a loss term that is proportional to the target atom

density n_0 , velocity of the incident electron, and the collisional cross section σ at the energy ϵ . The gain term should exactly balance the loss term at $\epsilon + \Delta\epsilon$ to conserve particles. Writing this operator for the distribution over energy first for a single excitation process j in eq. 6.17, and will then be converted to velocity and all processes.

$$C_{exc}^j(\epsilon) = n_0 \left[\sqrt{2 \frac{\epsilon + \Delta\epsilon^j}{m_e}} \sigma_{exc}^j(\epsilon + \Delta\epsilon^j) f_{\epsilon + \Delta\epsilon^j} - \sqrt{2 \frac{\epsilon}{m_e}} \sigma_{exc}(\epsilon) f_{\epsilon} \right] \quad (18.17)$$

Converting this operator to velocity space brings in a factor of $4\pi v^2$ due to the angular integrals of velocity, and also a factor of $\frac{dv}{d\epsilon} = \frac{1}{m_e v}$ due to the conversion of the distribution to velocity from energy to give $f_{\epsilon} = \frac{4\pi v}{m_e} f_v$. The conversion of C_{exc} is the same, and so all factors cancel except the ratios of the velocity in 6.18. The total excitation operator is then the sum of all the individual excitation processes to be included.

$$C_{exc}^j(v) = n_0 \left[\frac{v_*^2}{v} \sigma_{exc}^j(v_*) f_{v_*} - v \sigma_{exc}(v) f_v \right] \quad (18.18)$$

$$v_* = \sqrt{v^2 + 2\Delta\epsilon^j/2}$$

$$C_{exc}(v) = \sum_{j=1}^N C_{exc}^j(v) \quad (18.19)$$

The ionization operator is a bit trickier because in the absence of a differential cross-section, some assumption must be made about how the incident electron and the ejected electron share the total available kinetic energy. All that can be said for sure is

that the total energy is conserved: $\epsilon_f^a + \epsilon_f^b = \epsilon_i^a - I$. ϵ^a is the kinetic energy of the incident electron, ϵ^b is the energy of the ejected electron, and I is the ionization energy.

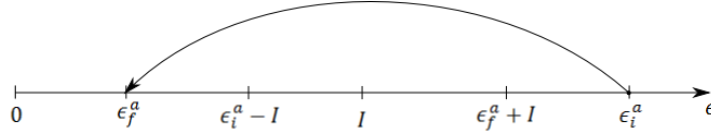


Figure 6.1 Energy diagram of inelastic scattering from ionization.

Reference [#] discusses the effect of different distributions of energy between the two electrons. For ease of implementation, a symmetric sharing of energy was used, where the incident electron has an equal probability of ending with any energy in the range , and the ejected electron has the remaining energy. That is, the probability of the incident electron landing in the range $\epsilon_f^a + d\epsilon$ is $P = \frac{d\epsilon}{\epsilon_i^a - I}$, if the final energy is in the range $0 \leq \epsilon_f^a \leq \epsilon_i^a - I$, and zero otherwise.

Electrons landing at a particular ϵ_f^a can only come from energies in the range $\epsilon_f^a + I \leq \epsilon_i^a < \infty$. The total rate of electrons landing at ϵ_f^a is found by integrating the collision rate, $f(\epsilon_i^a) \sqrt{2 \frac{\epsilon_i^a}{m_e}} \sigma_{ion}(\epsilon_i^a)$, over that entire valid range, weighted by the probability. If the ejected electron has the same distribution, then the total gain rate is simply twice that due only to the incident electron, which is what gives rise to particle imbalance. The loss rate is simply the ionization collision rate similar to eq. 6.17. The operator in energy space is given in 6.20, and converted to the velocity space in 6.21.

$$C_{ion}(\epsilon) = n_0 \left[2 \int_{\epsilon+I}^{\infty} d\epsilon' \sqrt{\frac{2\epsilon'}{m_e}} \frac{\sigma_{ion}(\epsilon') f_{\epsilon'}}{\epsilon' - I} - \sqrt{\frac{2\epsilon}{m_e}} \sigma_{ion}(\epsilon) f_{\epsilon} \right] \quad (18.20)$$

$$C_{ion}(v) = n_0 \left[\frac{2m_e}{v} \int_{v_*}^{\infty} dv' v'^3 \frac{\sigma_{ion}(v') f_{v'}}{\frac{1}{2}m_e v'^2 - I} - v \sigma_{ion}(v) f_v \right] \quad (18.21)$$

$$v_* = \sqrt{v^2 + 2I/m_e}$$

6.4 ENERGY AND PARTICLE BALANCE

Both inelastic operators do not conserve energy, and the ionization operator does not conserve particles. In order to find some steady state solution, the energy loss and particle gain must be balanced somehow by adding energy to the distribution, and including some kind of particle loss. The particle gain from ionization is found from the 1st order moment of the ionization operator as in eq. 6.22.

$$\frac{\partial n_e}{\partial t} = \int_0^{\infty} dv (4\pi v^2) C_{ion}(v) \quad (18.22)$$

To balance this, a particle loss term was added of the form $\frac{\partial f_v}{\partial t} = -L f_v$, where L would be some constant with units of s^{-1} . A physical particle loss would come from streaming resulting from spatial gradients of the distribution. L could represent some average loss process that has been averaged over all directions and velocities. The magnitude of L though has to be chosen to balance particle gain from ionization. Using the 1st order moment of the ionization operator gives the required magnitude of L in eq. 6.23.

$$L = \frac{1}{n_e} \int_0^{\infty} dv (4\pi v^2) C_{ion}(v) \quad (18.23)$$

The power loss density is found by taking a 2nd order moment of all the operators as in 6.24. The particle loss operator has to be included since it also does not conserve energy either.

$$\frac{\partial w_e}{\partial t} = \int_0^\infty dv \left(\frac{1}{2} m_e v^2 \right) (4\pi v^2) [C_{exc}(v) + C_{ion}(v) - Lf_v] \quad (18.24)$$

To balance energy loss, diffusion in velocity space is added to effectively heat the distribution: $D_{hot} \nabla_v^2 f_v$. The effect is similar to the existence of a shell of hot electrons surrounding the bulk distribution, which causes heating for the slower electrons. Instead of adding this second population at some arbitrary energy, a constant diffusion coefficient is used which would represent the population at infinity. Similar to 6.23, the magnitude of D_{hot} has to be found to balance energy loss in eq 6.24.

$$D_{hot} = - \frac{\int_0^\infty dv \left(\frac{1}{2} m_e v^2 \right) (4\pi v^2) [C_{exc}(v) + C_{ion}(v) - Lf_v]}{\int_0^\infty dv \left(\frac{1}{2} m_e v^2 \right) (4\pi v^2) \frac{1}{v^2} \frac{\partial}{\partial v} v^2 \frac{\partial f_v}{\partial v}} \quad (18.25)$$

This should fix both energy and particle balance, since the added diffusion still conserves particles. The full equation to be solved is the sum of all the operators and equating to zero in eq. 6.26.

$$C = C_{ee}(v) + C_{exc}(v) + C_{ion}(v) - Lf_v + D_{hot} \frac{1}{v^2} \frac{\partial}{\partial v} v^2 \frac{\partial f_v}{\partial v} \quad (18.26)$$

6.5 NUMERICAL SOLUTION FOR ARGON I

The atomic data used comes from the same model by Bogaerts et al.^[4] used in chapter four since it provides the collision cross sections for excitations from the ground state. Transitions between levels are not included since the excited state population

densities are many orders of magnitude lower than the ground state. The density for Ar II is also much lower than that of Ar I by about one order.

The solution was computed numerically. Velocity was discretized up to a maximum velocity of $v_{max} = 5v_{th} = 5\sqrt{2\frac{T_e}{m_e}}$, with 500 divisions. This value was determined empirically. A low value of v_{max} was found to cause the tail of the distribution to blow up. Also, a larger number of divisions per unit velocity required shorter time-steps to be numerically stable. A time step of $\Delta t = 1E - 11$ s was used.

The distribution was initially set to a Maxwellian of the desired temperature. It was then stepped in time using the total collision operator $\frac{\partial f}{\partial t} = C(v)$ that was derived. The characteristic time of change of the distribution was defined as $\frac{1}{\tau} = \frac{1}{n_e} \int (4\pi v^2) |C(v)|$. When this timescale reached $\tau \geq 20ms$, the resulting distribution was taken as the solution since this is much longer than the expected confinement time of the Helimak on the order of $1ms$.

Each time-step was computed using a linear explicit step (eq. 6.27). The integrals in the operators were not computed every time-step, but every 10-100 steps, to speed calculation.

$$f_v(v, t_{i+1}) = f_v(v, t_i) + \Delta t C(v, t_i) \quad (18.27)$$

Integrals were computed using a three-point Simpson's method (eq. 6.28). First derivatives were computed using a four-point method (eq. 6.29). Second derivatives were computed using a five-point method (eq. 6.30).

$$F_i = \frac{\Delta v}{3} (f_{i-2} + 4f_{i-1} + f_i) + F_{i-2} \quad (18.28)$$

$$\frac{\partial f_i}{\partial v} = \frac{1}{12\Delta v} (f_{i-2} - 8f_{i-1} + 8f_{i+1} - f_{i+2}) \quad (18.29)$$

$$\frac{\partial^2 f_i}{\partial v^2} = \frac{1}{12(\Delta v)^2} (-f_{i-2} + 16f_{i-1} - 30f_i + 16f_{i+1} - f_{i+2}) \quad (18.30)$$

An example solution is plotted in figures 6.2 and 6.3 in comparison to a Maxwellian distribution of the same temperature. A high neutral density was used for this example to exaggerate any differences. The solution distribution has a much higher value near $v = 0$. All electrons born of ionization appear there, and those that lose energy from due to inelastic collisions land there as well.

The depression of the distribution at higher velocities is not as obvious. In the log plot of the distribution, a depression can be seen between about 10eV and 50eV. Above 50eV it appears to develop a higher tail, which is due to the heating mechanism introduced to balance power loss.

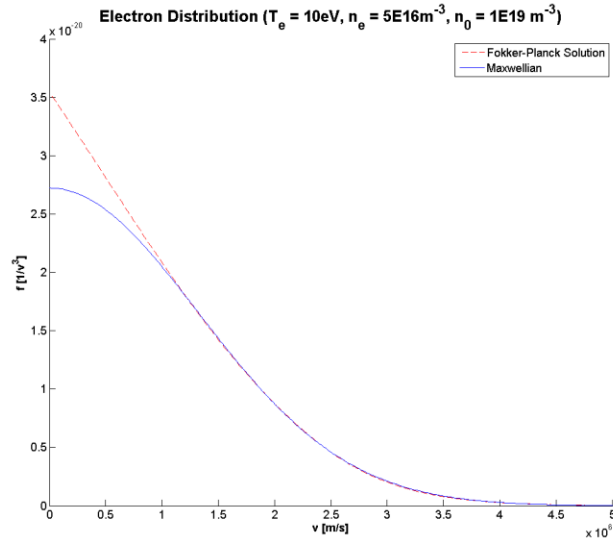


Figure 6.2 Solution electron velocity distribution $f_v(v)$ compared to a Maxwellian at the effective temperature.

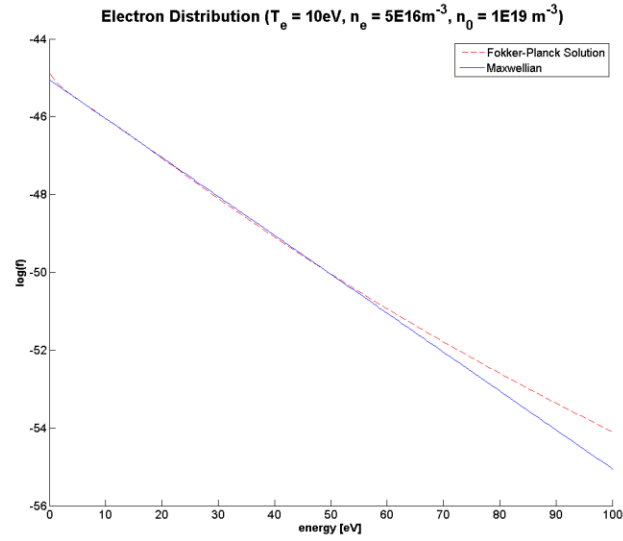


Figure 6.3 The distribution in $\log f_v$ versus $\epsilon = \frac{1}{2}m_e v^2$

6.6 CORRECTION FACTORS

The difference in excitation rates due to the deviation from Maxwellian should be proportional to the difference in the number of electrons above the threshold energy of the collisional process in question. If there is the same number of electrons above 15.8eV, for example, then the ionization rate of Argon I will be nearly unaffected. A correction factor is defined in eq. 6.31 by taking this ratio of the total number of electrons above a certain energy, where f_{IE} is the solution to the model including inelastic collisions and f_{Max} is a Maxwellian distribution.

$$C_{\epsilon} = \frac{\int_{\epsilon}^{\infty} d\epsilon' f_{IE}(\epsilon')}{\int_{\epsilon}^{\infty} d\epsilon' f_{Max}(\epsilon')} \quad (18.31)$$

These coefficients were tabulated for three difference energies. Excitation rates for the observed lines of Argon I were corrected using $\epsilon = 11.5eV$ as the threshold energy. Ionization rates of Argon I used $\epsilon = 15.8eV$. Excitation rates for the lines of Argon II used a threshold energy of $\epsilon = 19.2eV$. Solutions were calculated for electron temperatures of 5, 10 and 20eV, except for the ArI rates, where only 10 and 20eV are given. Electron densities of 1, 2, 5, 10, 20, 50, 100 and $200 \times 10^{16}m^{-3}$, which relate to the tables 4.1 and 4.2. These results are given in tables 6.1, 6.2 and 6.3. Neutral density values of 1, 2, 5, and $10 \times 10^{17}m^{-3}$ are used.

Temperatures of 0.5, 1, and 2 eV are not given, and 5eV for ArI, because their correction factors did not deviate from unity. It is believed that this is because only the tail of the distribution is being sampled. The heating operator and the inelastic collision operators seem to balance the other's effect for these energies.

$n_e[m^{-3}]$ $T_e[eV]$	1.00E+16	2.00E+16	5.00E+16	1.00E+17	2.00E+17	5.00E+17	1.00E+18	2.00E+18
$n_{ArI} = 1 \times 10^{17} m^{-3}$								
10	0.99	0.99	1	1	1	1	1	1
20	0.95	0.96	0.97	0.98	0.99	0.99	1	1
$n_{ArI} = 2 \times 10^{17} m^{-3}$								
10	0.99	0.99	0.99	1	1	1	1	1
20	0.95	0.95	0.96	0.97	0.98	0.99	0.99	1
$n_{ArI} = 5 \times 10^{17} m^{-3}$								
10	0.99	0.99	0.99	0.99	0.99	1	1	1
20	0.94	0.95	0.95	0.96	0.96	0.98	0.98	0.99
$n_{ArI} = 1 \times 10^{18} m^{-3}$								
10	0.99	0.99	0.99	0.99	0.99	0.99	1	1
20	0.94	0.94	0.95	0.95	0.96	0.97	0.98	0.98

Table 6.1 Argon I Excitation Rate Corrections ($\epsilon = 11.5eV$)

$n_e[m^{-3}]$ $T_e[eV]$	1.00E+16	2.00E+16	5.00E+16	1.00E+17	2.00E+17	5.00E+17	1.00E+18	2.00E+18
$n_{ArI} = 1 \times 10^{17} m^{-3}$								
5	0.96	0.98	0.99	1	1	1	1	1
10	0.99	0.99	0.99	1	1	1	1	1
20	0.93	0.94	0.95	0.96	0.98	0.99	0.99	1
$n_{ArI} = 2 \times 10^{17} m^{-3}$								
5	0.93	0.96	0.98	0.99	0.99	1	1	1
10	0.98	0.99	0.99	0.99	1	1	1	1
20	0.92	0.93	0.94	0.95	0.96	0.98	0.99	0.99
$n_{ArI} = 5 \times 10^{17} m^{-3}$								
5	0.86	0.91	0.95	0.97	0.99	0.99	1	1
10	0.98	0.98	0.98	0.99	0.99	1	1	1
20	0.92	0.92	0.93	0.93	0.95	0.96	0.98	0.99
$n_{ArI} = 1 \times 10^{18} m^{-3}$								
5	0.8	0.86	0.92	0.95	0.97	0.99	0.99	1
10	0.98	0.98	0.98	0.98	0.99	0.99	1	1
20	0.92	0.92	0.92	0.93	0.93	0.95	0.96	0.97

Table 6.2 Argon II Excitation Rate Corrections ($\epsilon = 19.2eV$)

$n_e[m^{-3}]$ $T_e[eV]$	1.00E+16	2.00E+16	5.00E+16	1.00E+17	2.00E+17	5.00E+17	1.00E+18	2.00E+18
$n_{ArI} = 1 \times 10^{17} m^{-3}$								
5	0.98	0.99	1	1	1	1	1	1
10	0.99	0.99	0.99	1	1	1	1	1
20	0.94	0.94	0.96	0.97	0.98	0.99	0.99	1
$n_{ArI} = 2 \times 10^{17} m^{-3}$								
5	0.97	0.98	0.99	1	1	1	1	1
10	0.99	0.99	0.99	0.99	1	1	1	1
20	0.93	0.94	0.95	0.96	0.97	0.98	0.99	0.99
$n_{ArI} = 5 \times 10^{17} m^{-3}$								
5	0.95	0.97	0.98	0.99	1	1	1	1
10	0.98	0.98	0.99	0.99	0.99	1	1	1
20	0.93	0.93	0.94	0.94	0.95	0.97	0.98	0.99
$n_{ArI} = 1 \times 10^{18} m^{-3}$								
5	0.92	0.94	0.97	0.98	0.99	1	1	1
10	0.98	0.98	0.98	0.99	0.99	0.99	1	1
20	0.93	0.93	0.93	0.93	0.94	0.95	0.97	0.98

Table 6.3 Argon I Ionization Rate Corrections ($\epsilon = 15.8eV$)

Chapter 7: Spectroscopic Profiles for n_e and T_e

7.1 PROFILE CALCULATION

A profile for n_e and T_e by spectroscopic measurements is only possible over the ~35cm viewing range of the viewport. Each measurement consisted of one shot on the Helimak, with several integrations averaged and processed as described in chapter 3. Spectroscopic measurements were taken at 1cm increments for a total of 34 different positions.

The methods in chapter 4 were then used to determine a value of n_e and T_e at each position, including the correction factors calculated in chapter 6, and initially assuming a flat density profile for the ground level of neutral Argon equal to the pressure recorded from the ionization gauge. The peak value of n_e and T_e were used with the kinetic model developed in chapter 5 to give a new density profile for the neutral Argon. The new neutral profile was then used to calculate new values of n_e and T_e . This process was repeated until the profiles of n_e , T_e , and n_{ArI} gave self-consistent results.

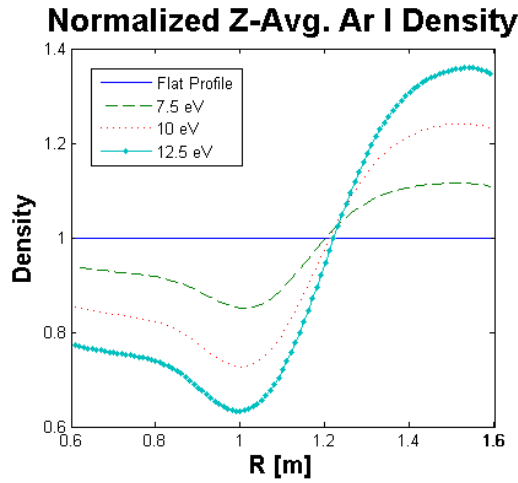


Figure 7.1 Profiles of Ar I calculated for three different peak electron temperatures and densities using the kinetic model of chapter 5.

Figure 7.1 shows several profiles for Ar I at several different values of n_e and T_e . They are labeled primarily by T_e , since the resulting peak electron density does not change significantly for each neutral profile. The peak values used for the fitting functions in chapter 5 were determined by trial and error, and in the end there seems to be only rough agreement.

The resulting spectroscopic profiles for n_e and T_e are shown in figure 7.2. None of the profiles exactly reproduce the values used for Ar I model calculations, but the 10eV profile seems to be the closest if only an averaged peak values is taken, which would agree roughly with probe measurements of T_e . The n_e profiles are more striking since the peak values are seemingly insensitive to the neutral profile, and are also 2 to 3 times higher in magnitude than the probe value of about $2.5E16m^{-3}$.

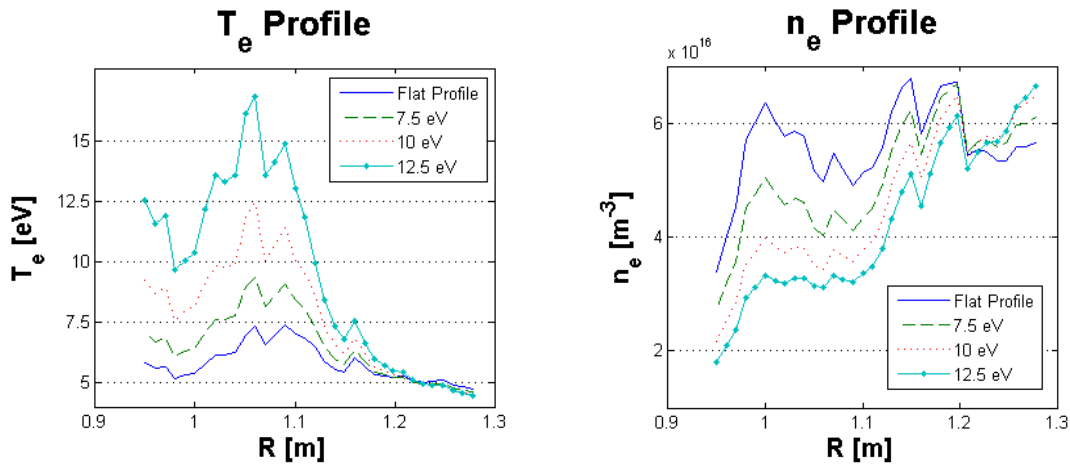


Figure 7.2 n_e and T_e using the spectroscopic measurements and neutral profiles in figure 7.1. The closest match is the 10eV profile, giving an average peak T_e of about 11eV.

7.2 DISCUSSION

Using spectroscopic measurements of neutral Argon has proven to be very tricky due to its high ionization cross section and resulting depletion within the plasma. Even though there does appear to be better consistency then with previous attempts, the method presented here still does not appear to solve all inconsistency problems. The fitting functions used in chapter 5 are probably insufficient since the resulting profile for n_e appears to have a completely different shape. The neutral profiles are also sensitive to the source profile used, which is not really known. The breaking of the axial and vertical symmetries due to the termination of the plasma on the bias plates may also be causing inconstancy.

Even though the shape of the electron density may be incorrect, it does seem to indicate a much higher peak electron density than probe measurements.

Appendix (or Appendices)

This page is optional—must be placed in this order if it is included in the thesis. If you don't want to include an appendix, then delete the entire page and the following page break.

Glossary

This page is optional—must be placed in this order if it is included in the thesis. If you don't want to include a glossary, then delete this entire page and the following page break.

References

- [1] Griem, H. R. (1997). *Principles of Plasma Spectroscopy* (Cambridge University Press, New York)
- [2] Hazeltine, R. D. and Waelbroeck, F. L. (2004). *The Framework of Plasma Physics* (Westview Press, Boulder)
- [3] K. Gentle, H. He, Texas Helimak. *Plasma Sci. and Tech.* **10** (3) (2008)
- [4] A. Bogaerts, R. Gijbels, J. Vlcek, Collisional-radiative model for an argon glow discharge. *J. Appl. Phys.* **84** (1), 121-136 (1998)
- [5] E. M. Sciamma, Plasma Spectroscopic Diagnostic Tool Using Collisional-Radiative Models and its Application to Different Plasma Discharges For Electron Temperature and Neutral Density Determination, U. Texas Austin Dissertation (2007)
- [6] Ocean Optics Red Tide USB650 Fiber Optic Spectrometer Installation and Operation Manual
- [7] <http://www.mksinst.com/docs/ur/GaugeGasCorrection.aspx>
- [8] <http://www.nist.gov/pml/data/asd.cfm>
- [9] National Instruments USB-6008 Bus-Powered Multifunction DAQ USB Device User Guide
- [10] J. Vlček, A collisional-radiative model applicable to argon discharges over a wide range of conditions I: Formulation and basic data. *J. Phys. D: Appl. Phys.* **22**, 623-631 (1989)
- [11] J. Vlček, V. Pelikán, A collisional-radiative model applicable to argon discharges over a wide range of conditions II: Application to low-pressure, hollow-cathode arc and low-pressure glow discharges, *J. Phys. D: Appl. Phys.* **22**, 632-643 (1989)
- [12] M. Arnaud, R. Rothenflug, An updated evaluation of recombination and ionization rates, *Astron. Astrophys. Suppl. Ser.* **60**, 425-457 (1985)
- [13] J. D. Huba (2009) *NRL Plasma Formulary* (Naval Research Laboratory, Washington, DC)

Vita

<This page is optional: If you do not include a Vita, delete this entire page. The Vita is a brief biographical sketch of the writer that provides information for future readers. It should include the writer's full name and a permanent address or e-mail address where he or she can be reached. Because the thesis/report will be available electronically, be aware that certain personal information could be used to steal your identity. For this reason, you are advised not to include your date of birth, parents' names, or children's names. The name of the typist should always appear at the end of the page.>

Permanent address (or email): <nn Street Name, City, State Zip>

This thesis (report) was typed by <the author, or typist's name>.